REVERSE TIME MIGRATION AND FULL WAVEFORM INVERSION IN RIEMANNIAN MANIFOLDS: APPLICATION TO RUGGED TOPOGRAPHY

A Dissertation

Presented to the Instituto de Física

of Universidad de Antioquia

in Partial Fulfillment of the Requirements for the Degree of

Doctor en Física

Advisor: Ph.D. Luis Duque

by

Cesar Arias

October 2017

REVERSE TIME MIGRATION AND FULL WAVEFORM INVERSION IN RIEMANNIAN MANIFOLDS: APPLICATION TO RUGGED TOPOGRAPHY

Cesar Arias, MSc

University of Antiquia 2017

Reverse Time Migration (RTM) and Full Waveform Inversion (FWI) are techniques widely used in the hydrocarbon exploration industry to generate images of the earth's sub-surface at target depths by means of controlled seismic waves. The first technique produces reflectivity maps that show the distribution of the structures under the surface and the second gives information about parameters that can model the earth's properties.These parameters are for example wavespeed, density, or other elastic parameters of the media. Both techniques have been traditionally applied to zones with flat surface, and in order to adapt them to zones of complex topography some geometrical transformations have been proposed recently that translate the RTM and FWI algorithms to a Riemaniann scenario. We introduce a simple type of geometrical transformation to implement these algorithms for rugged topography, analyze the stability conditions for these scenarios and analyze its consequences in terms of computational cost as compared with non-Riemannian case.

”We are at the very beginning of time for the human race. It is not unreasonable that we grapple with problems. But there are tens of thousands of years in the future. Our responsibility is to do what we can, learn what we can, improve the solutions, and pass them on”.

Richard P. Feynman

ACKNOWLEDGEMENTS

This work has been possible thanks to the financial support given by the colombian oil company ECOPETROL and COLCIENCIAS within the program 0266-2013: *Migración sísmica preapilado en profundidad por extrapolación de campos de onda utilizando computación de alto desempeño para datos masivos en zonas complejas*. ITM cod.: P12102. We also thank the team of the Laboratory of High Performance Geophysics at the University of Campinas, Brazil for the opportunity of a two-month stay and helpful discussions and advice.

TABLE OF CONTENTS

INTRODUCTION

RTM is an imaging technique that although was introduced in the year 1983 (E. Baysal and Sherwood, 1983) has only been extensively used in the last few years because the computational resources needed to implement it were only available recently. Despite its high computational cost, RTM is nowaday's choice among a wide set of options to produce seismic images because it can be used in zones with strong variations of the velocity of propagation, it can map sub-surface structures with any dipping angle and can create good images of zones of interest like those under and around salt domes where hydrocarbon reservoirs can be found.

The classical RTM algorithm produces images of the earth's sub-surface by means of controlled seismic waves. These waves are generated mechanically using seismic sources such as vibroseis (a truck-mounted vibrator) or controlled explosions among others. Figure 1 (Sahara Wealth Advisors, 2015) shows a typical field setup used to get the seismic data, required as the starting point for the RTM method.

The wavefield registered by each geophone is known as *trace*. When all traces are put together, in some order, the result is called *seismogram* where the horizontal axis (in units of lenght), corresponds to a coordinate in which the geophones are placed and the vertical axis is the time (Figure 2).

The signal contained in each trace can be *retropropagated* in order to map the

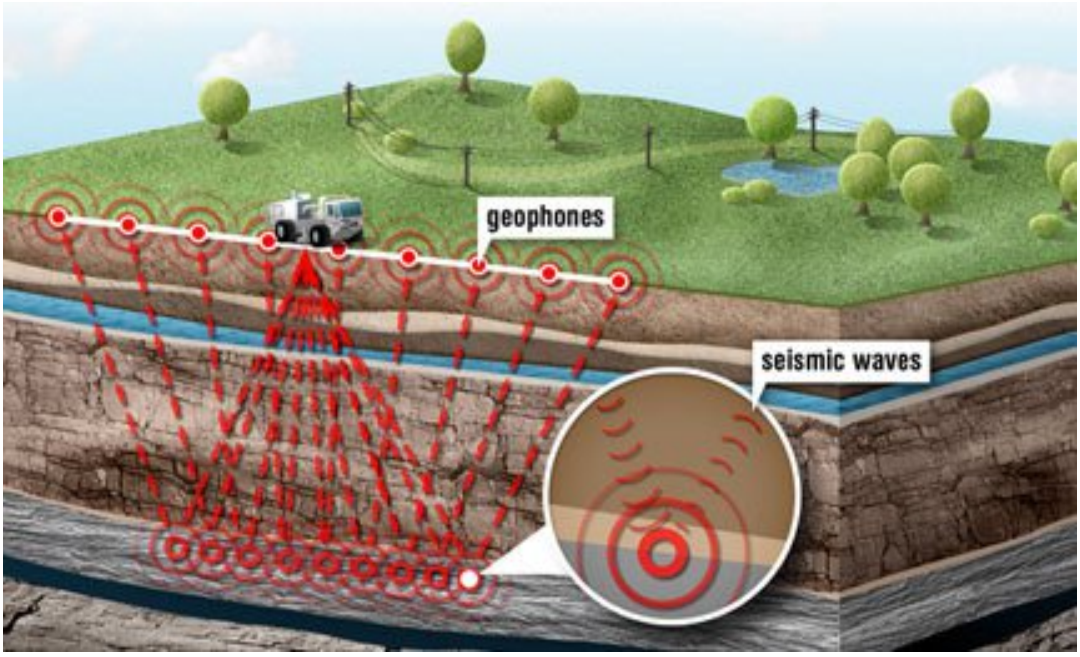

Figure 1: Typical scheme for the acquisition of seismic waves used in the RTM method. The geophones are devices similar to microphones that register the seismic waves that carry information of the internal structures of the earth since they are reflected in the interfaces of strata

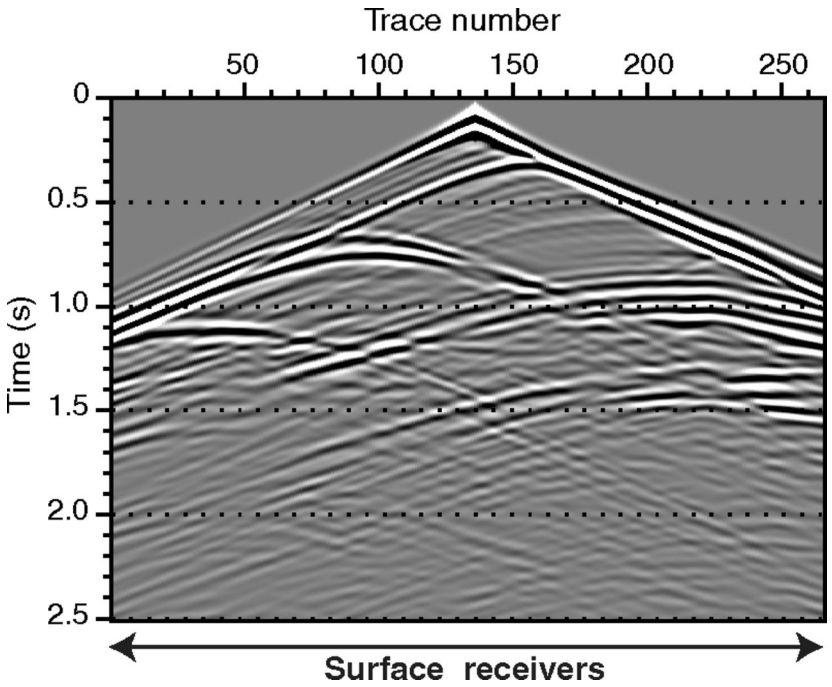

Figure 2: Typical form of a seismogram

regions of the sub-suface where reflected energy came from. This procedure is done using the wave equation (acoustic or elastic) where the trace (inverted in time) enters as the source term. When this propagation procedure is done with all seismic traces simulaneously, it produces what is known as *backpropagated wavefield*, $P_b(x, y, z, t)$, where x, y and z are the spatial coordinates and t the time. This field carries information about the interfaces that produced the reflections. To create the RTM image, the simulation of the seismic source propagation is needed as well. The functional form of the artificial seismic pulse is modeled mathematically and introduced as the source term in the same wave equation used for the backpropagation. The result is the *forward propagated field*, $P_f(x, y, z, t)$. P_f and P_b should coincide in the regions of the sub-surface where the field was reflected (Figure 3).

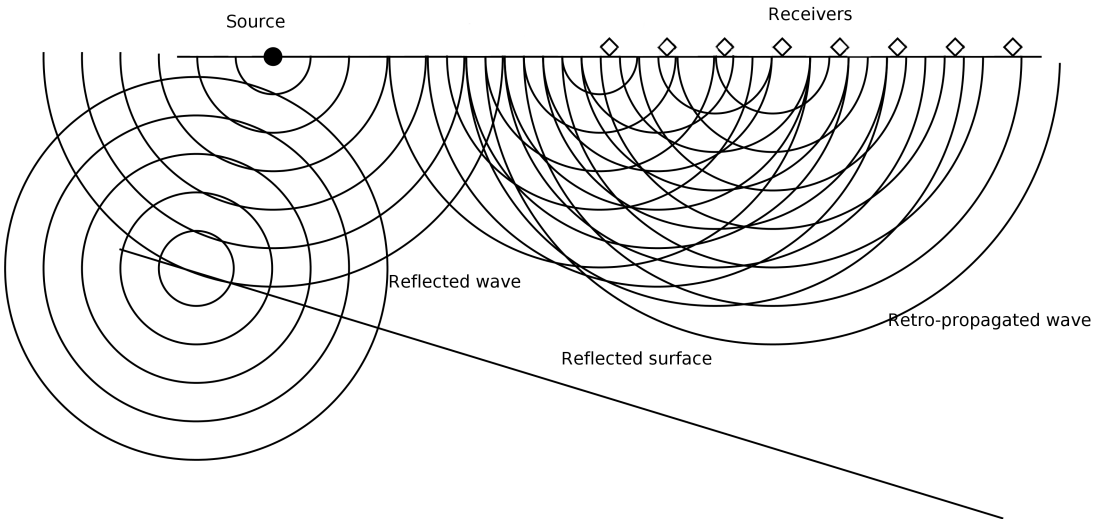

Figure 3: Graphical representation of the cross-correlation procedure. The forward propagated field and the backward propagated field should have a high cross-correlation in the regions where the waves are reflected

To map those reflecting regions, the zero-lag cross-correlation of the forward propagated field and the backward propagated field is calculated using the expression:

$$I(x, y, z) = \sum_{s} \sum_{r} \int dt P_f(z, y, z, t) P_b(z, y, z, t). \quad (1)$$

The result of the cross-correlation is the RTM image. A typical RTM image is shown in Figure 4.

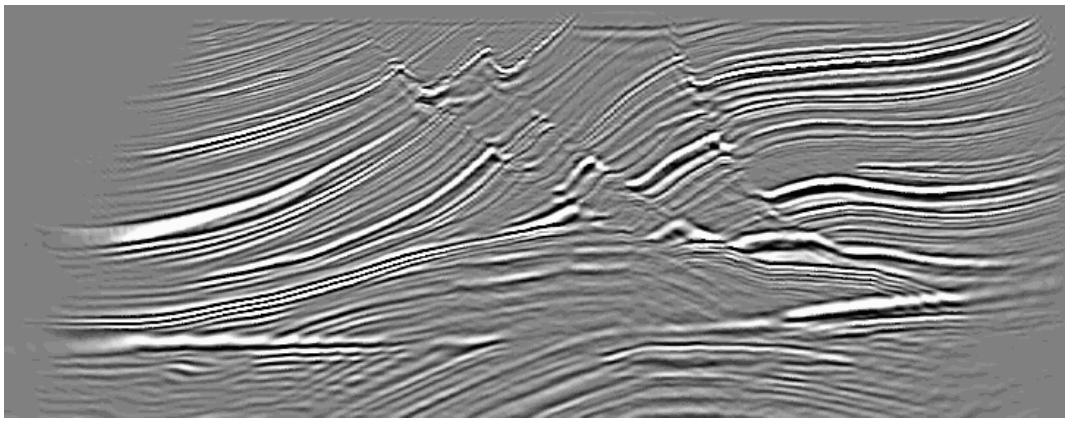

Figure 4: RTM image for the Marmousi synthetic model

Before the use of RTM algorithms were popular, the most common technique used to produce seismic images were based on rays named the method Kirchhoff. Another commonly used method is known as One-Way Wave Equation, OWWE, or wave-field extrapolation since it takes the field that was registered in the surface by the seismic geophones and extrapolate it back into the earth's interior in order to predict the location of the reflecting structures or strata where the came from (Claerbout and Doherty, 1983; D. Loewenthal and Sherwood, 1976; Stolt, 1978). This method is much faster and require less memory but has some drawbacks: it can not handle media with strong horizontal variation in the wave speed and also fails to create good images in the regions of the earth's sub-surface where the strata have big dipping angles (Stolt, 1978). These zones

can be found in practice for example near faults, in over-thrusts, or under the salt domes and are of special interest in the hydrocarbon exploration industry because they can present oil traps (Figure 5). Since the OWWE method use approximated solutions to the wave equation in which the wavefield propagation is computed only in one direction (usually down), the zones under the salt domes as those that can be seen in Figure 5 (Energy education, 2015) can not be well illuminated.

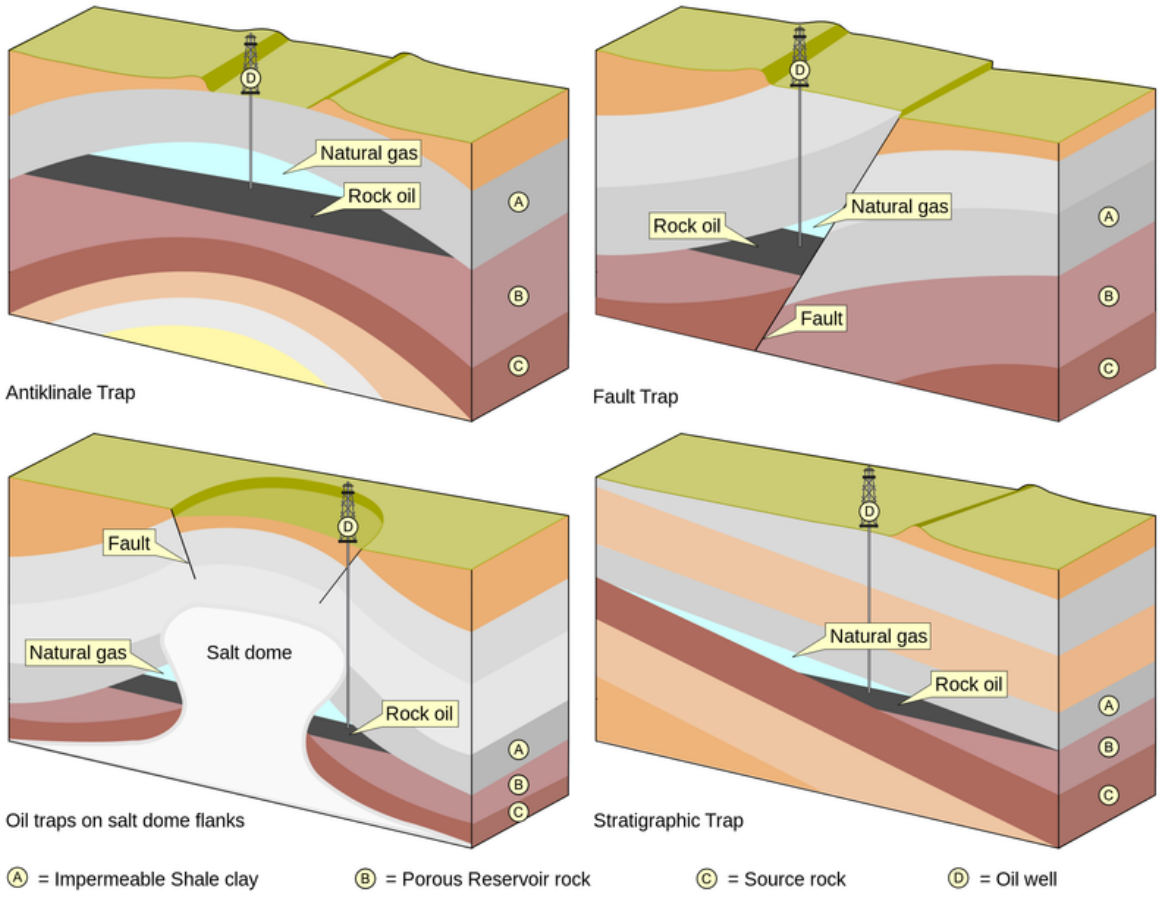

Figure 5: Different configurations of hydrocarbon traps presenting zones with large dipping angles.

In order to improve the illumination of the these zones, Sava and Fomel (2005) introduced a modification of the OWWE method consisting in taking the OWWE equations into a Riemannian scenario where the coordinate system used

is not Cartesian but curvilinear. This is achieved by modifying the Laplacian of the wave equation introducing a metric tensor. In this way Sava and Fomel obtained a one-way field extrapolation method that can be used to propagate the seismic waves in arbitrary directions, in contrast to downward continuation, which is used for waves propagating in the vertical direction. This semi-orthogonal coordinates systems includes for example the ray coordinate systems in which the wave propagation happens mainly along the extrapolation direction. The use of semi-orthogonal system of coordinates in this approach can lead to situations in which the coordinates system suffer from problematic bunching and singularities. To solve this problems Shragge (2008) introduced the non-orthogonal Riemannian field extrapolation, a procedure that introduces singularity-free coordinate meshes.

In the decade of 2010s the OWWE methods became less popular, mainly because the available computational resources made possible the use of more powerful methods such as RTM, which are based on the solution of the complete wave equation without the strong approximations required by the old field extrapolation method. The RTM method is better because the complete solution of the wave equation takes into account the up-going and down-going fields. and the large dips in the strata are also well imaged and RTM can handle any variation in the propagation velocity of the seismic waves. It seems then that there is no need to use non-orthogonal coordinates systems anymore to illuminate complex zones.

Nevertheless it has been pointed out recently (Shragge, 2014a) that the application of RTM method to zones with strong variations on the height (rugged topography) requires the forced application of a Cartesian mesh to a curved

domain. This can lead to a wrong positioning of sub-surface structures and gives rise to defects known as artifacts in the final images. In order to solve this problems, he proposed a coordinate transformation to turn the rugged acquisition surface into a flat one by means of a 2D complex variable transformation, namely, the Schwarz-Christoffel transformation. With this approach, the RTM algorithm is applied in a geometrically transformed domain in which the wave equation is changed into a more general equation and the metric of the space is no more Euclidean but Riemannian. In this way good RTM images are obtained but at the expense of increased computational time. Another inconvenience of this approach is that the Schwarz-Christoffel transformation can not be generalized to a 3D scenario. A more general approach was introduced (Shragge, 2014b) in which the Riemannian acoustic wave equation was solved for 3D domains. The next step pointed out by him was the implementation the complete RTM algorithm. Here we implement the RTM algorithm based in that type of transformations. We present a simple map that transforms a generally curved acquisition surface into a flat one. The curved domain is transformed into a rectangular domain where a uniform grid can be applied to solve the acoustic wave equation with a generalized Laplacian. When the 3 steps of the RTM are finished in this rectangular domain we map the final image into the curved domain, i.e., into the physical domain.

Another problem that can be taken into the Riemannian scenarios is the inversion of seismic data. Full waveform inversion or FWI (Tarantola, 1984) is a data-fitting method that uses an approximate velocity model estimate of the subsurface and iteratively finds a better estimate such that the quadratic error between modeled seismogram (computed with the estimated velocity model) and the observed seismogram decreases as the number of iterations increases.

There are several ways to update the estimate of the velocity model at each iteration, but one of the simplest and most efficient is the gradient descent method. The strategy proposed by Plessix (2006) can be used to compute the gradient via the adjoint state method. A good review for the FWI method was written by J. Virieux and S. Operto (2009).

Currently, the FWI method is an active research topic, from the mathematical, computational and geophysical points of view. Several drawbacks of this method still remain as open problems. Among others, the problem of avoiding local minima, the sensitivity of the method to amplitude errors (Virieux 2009) and high cost. In addition, Shragge (2014b), pointed out that the use of Riemannian manifolds for rugged topography would allow to obtain better estimates of model parameters at the near surface. We implemented a FWI algorithm in Riemannian coordinates based on the approach introduced by Shragge (2014). FWI methods for rugged topography (Y. Han and Jia, 2015) have been previously proposed for decoupled acoustic wave equation using a velocity model with simple topography and a different transformation. Here the FWI is implemented for the Canadian Foothills velocity model which is a standard SEG model useful to test algorithms for rugged topography. The results of our computational experiments show that our proposed approach makes feasible to perform FWI in domains with a general rugged surface. The computational cost is increased but the convergence of the method is quite good. Our approach estimates satisfying velocity models even for the near surface region where it is usually difficult to have good results.

The construction of images of the Earth's interior using methods like RTM

or FWI depends crucially on the numerical solution of the wave equation. A mathematical expression of the numerical stability and dispersion for a particular wave equation must be known in order to avoid unbounded numbers of amplitudes. In the case of the acoustic wave equation, the Courant-Friedrich-Lewy (CFL) condition is a necessary, but not a sufficient condition for convergence. Thus, we need to search other types of stability conditions.

Shragge (2014a) derived a stability condition in a heuristic way taking as a starting point the Courant stability condition and translating it to the transformed scenario by means of the chain rule of calculus. This is not formally a stability condition and indeed the resulting rule it gives to calculate the time sampling needed to ensure stability of the finite differences (FD) solution is quite far of being true. Appelo and Petersson (2009) established a second order stable finite difference scheme for the elastic wave equation in a curvilinear system, showing that the spatial operators in the method are self-adjoint for free-surface, nevertheless, the authors do not present a stability criteria. Recently in Zhao et al. (2014), the Von-Neumann method was applied to stability and numerical dispersion in a FD scheme for the diffusive-viscous wave equation. The results obtained were compared with stability for the acoustic case and revealed that the stability condition is more restrictive for the diffusive-viscous case on which a smaller time step is required. The numerical dispersion is also smaller than that in the acoustic case.

We applied the Von-Neumann method to obtain a stability criteria for a FD scheme, first for a second-order in time and second-order in space, and then for second order in time and fourth order in space, applied to the 2D Riemannian acoustic wave equation and compared it with the heuristic one used by Shragge

(2014a). For numerical comparison, we also performed a wave propagation experiment using two different topography profiles: a Gaussian 2D profile and the Canadian Foothills profile (Gray and Marfurt, 1995), a synthetic velocity model representing a zone in the British Columbia (Canada) that shows several geological complexities common in that region. This velocity model allows us to show the dependence of the stability criteria on the smoothness of the profile. Finally, we analyze the numerical dispersion for the generalized wave equation and compare it with the Cartesian acoustic wave equation.

CHAPTER 1

MATHEMATICAL FRAMEWORK

2D Riemannian Wave Equation

In this chapter we make a review of the formulation of the Riemannian wave equation which agrees with the wave equations used by Sava and Fomel (2005), Shragge (2008) and Shragge (2014a). For a basic study on Riemannian manifolds the reader is referred to Robin and Salamon (2013) and for elastic formulation on Riemannian manifolds see Marsden and Hughes (1983).

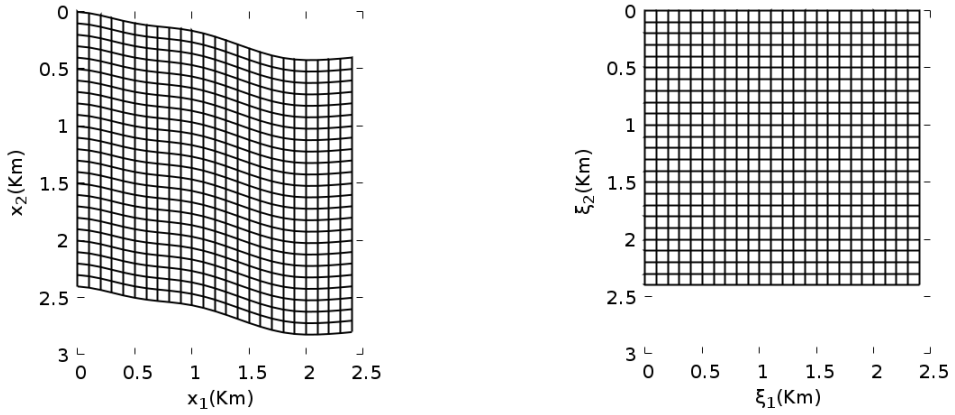

Figure 2.1. Physical domain (left) and computational domain (right).

Let $\mathbf{x} = [x_1, x_2]^T$ be the coordinates of a curved physical domain on which we want to solve the wave-equation and $\xi = [\xi_1, \xi_2]^T$ a regular (rectangular) computational domain on which one actually computes the acoustic wave field (Figure 1). Thus, we use a function $\mathbf{x} = \phi(\xi)$ that maps from computational domain onto physical domain. Hence, we have the (constant-density) acoustic wave equation in a 2D generalized coordinate system defined by

$$\nabla_\xi^2 U_\xi - \frac{1}{v_\xi^2}\frac{\partial^2 U_\xi}{\partial t^2} = F_\xi, \tag{1.1}$$

where $U_\xi = U(\phi(\xi), t)$ is a scalar wave field, the scalar $v_\xi = v(\phi(\xi))$ as the wave velocity and $F_\xi = F(\phi(\xi), t)$ is the source distribution. Hence, take the Jacobian of ϕ as

$$\mathbf{J} = \frac{\partial \phi}{\partial \xi}\,, \tag{1.2}$$

the Laplace-Beltrami operator ∇^2_ξ is described as (Guggenheimer, 1977)

$$\nabla^2_\xi = \sum_{j=1}^{2}\sum_{l=1}^{2} \frac{1}{\sqrt{|\mathbf{g}|}} \frac{\partial}{\partial \xi_j}\left(g^{jl}\sqrt{|\mathbf{g}|}\frac{\partial}{\partial \xi_l}\right), \tag{1.3}$$

where $|\mathbf{g}| = \det[g_{jl}]$ is the determinant of g_{jl} with

$$[g_{jl}] = \mathbf{J}^T\mathbf{J} \quad \text{and} \quad [g^{jl}] = \left[g_{jl}\right]^{-1}\,. \tag{1.4}$$

Thus, take the coordinate transformation mapping ϕ as a diffeomorphism (it is an invertible and smooth function whose inverse is smooth too) the basic question on that manifold is its Jacobian $\mathbf{J}$ preserves area (volume). That is,

$$\det[\mathbf{J}] = 1\,, \quad \text{that implies} \quad |\mathbf{g}| = 1\,. \tag{1.5}$$

Equation (1.5) makes the Laplace-Beltrami operator a good candidate to formulate acoustic wave equations on a Riemannian manifold. Note that the transformation ϕ is a mapping that transforms from computational domain to the physical domain in a bijective way, preserving the area, and, at least, twice differentiable. Using that transformation, we find a new expression for the Laplacian-Beltrami operator on the computational domain ξ to propose an acoustic wave equation.

Expanding the Laplacian, equation (1.3), we can write it in a more convenient way, as

$$\nabla^2_\xi = \sum_{j=1}^{2}\sum_{l=1}^{2}\left[g^{jl}\frac{\partial^2}{\partial \xi_j \partial \xi_l}\right] + \zeta^1\frac{\partial}{\partial \xi_1} + \zeta^2\frac{\partial}{\partial \xi_2}\,, \tag{1.6}$$

and as $\sqrt{|\mathbf{g}|} = 1$, where

$$\zeta^l = \sum_{j=1}^{2} \frac{\partial g^{jl}}{\partial \xi_j}\,. \tag{1.7}$$

Therefore, using Equation (1.6) in Equation (1.1), we have the generalized acoustic 2D wave equation given by

$$\left[g^{11}\frac{\partial^2 U_\xi}{\partial \xi_1^2} + 2g^{12}\frac{\partial^2 U_\xi}{\partial \xi_1 \partial \xi_2} + g^{22}\frac{\partial^2 U_\xi}{\partial \xi_2^2} + \zeta^1\frac{\partial U_\xi}{\partial \xi_1} + \zeta^2\frac{\partial U_\xi}{\partial \xi_2} \right] - \frac{1}{v_\xi^2}\frac{\partial^2 U_\xi}{\partial t^2} = F_\xi. \tag{1.8}$$

Surface topography problem

Using the coordinate transformation approach allows to compute directly the acoustic wave propagation in topographic coordinates.

The transformation that maps the rectangular domain with coordinates onto the physical domain is given by

$$\begin{cases} x_1 &=& \phi_1(\xi_1, \xi_2) &=& \xi_1\,; \\ x_2 &=& \phi_2(\xi_1, \xi_2) &=& \xi_2 + \psi(\xi_1)\,, \end{cases} \tag{1.9}$$

where ψ is a smooth function that represents the curved upper boundary of the physical domain. This function must be, at least, twice differentiable. Thus, under that condition the function $\phi = (\phi_1, \phi_2)$ is a coordinate chart for the physical domain which is being modeled on a regular Euclidean space (see, Figure 2.1. The elements $\zeta^{\mathbf{i}}$ are geometric factors as the $g's$ so they have to be calculated only once. For our specific transformation, given in Equation (1.9), we have:

$$[g_{ij}] = \begin{bmatrix} \left(1 + (\psi')^2\right) & \psi' \\ \psi' & 1 \end{bmatrix}, \quad [g^{ij}] = \begin{bmatrix} 1 & -\psi' \\ -\psi' & (1 + (\psi')^2) \end{bmatrix} \quad \text{and} \quad |\mathbf{g}| = 1\,. \tag{1.10}$$

The ζ^j coefficients are explicitly given by

$$\begin{aligned} \zeta^1 &= \frac{\partial g^{11}}{\partial \xi_1} + \frac{\partial g^{12}}{\partial \xi_2} = 0\,, \\ \zeta^2 &= \frac{\partial g^{21}}{\partial \xi_1} + \frac{\partial g^{22}}{\partial \xi_2} = -\psi''\,. \end{aligned} \tag{1.11}$$

Therefore, using equations (1.10)-(1.11) in Equation (1.8), we arrive in

$$\left[\frac{\partial^2 U_\xi}{\partial \xi_1^2} - 2\psi' \frac{\partial^2 U_\xi}{\partial \xi_1 \partial \xi_2} + \left[1 + (\psi')^2\right] \frac{\partial^2 U_\xi}{\partial \xi_2^2} - \psi'' \frac{\partial U_\xi}{\partial \xi_2}\right] - \frac{1}{v_\xi^2} \frac{\partial^2 U_\xi}{\partial t^2} = F_\xi\,, \tag{1.12}$$

noting that ψ' and ψ'' are functions of ξ_1.

1.1 2D-second order Riemannian wave equation FD scheme

The finite-difference method is the most straightforward numerical approach in seismic modeling due to its relative accuracy and computational efficiency. Nevertheless, the size of the time step is bounded by a stability criterion which is an important factor affecting the accuracy of the results. This bound depends on the grid spacing and particularly, for the riemannian 2D wave equation, it also depends on geometrical factors.

Von-Neumann stability criteria of Riemannian 2D wave equation

The stability condition for the acoustic wave equation is widely known as the Courant-Friderichs-Lewy condition (CFL) and is given in the case of two spatial dimensions by

$$\Delta t \leq \frac{\Delta r}{v(\mathbf{x})}, \tag{1.13}$$

where

$$\Delta r = \left[\Delta x_1^{-2} + \Delta x_2^{-2}\right]^{-\frac{1}{2}} \tag{1.14}$$

is the root-mean-square (RMS) of the spatial sampling and $v(\mathbf{x})$ is the maximum value of the velocity model in physical grid.

In the Riemannian case the only approach to it has been made by Shragge (2014b) who uses the chain rule to go from Equation (1.13) to the following expression (that from now we will call *heuristic limit*):

$$\Delta t \leq \frac{1}{v_\xi} \times \underset{\xi}{\operatorname{argmin}} \left\{ \left[\left(\frac{\partial \phi_1}{\partial \xi^T} \Delta \xi \right)^{-2} + \left(\frac{\partial \phi_2}{\partial \xi^T} \Delta \xi \right)^{-2} \right]^{-\frac{1}{2}} \right\} . \tag{1.15}$$

To derive the numerical stability condition we make use of the Von-Neumann method as follows:

The differential operators in Equation (1.8), expanded in a second order finite

difference scheme are:

$$\begin{aligned}
\frac{\partial^2 U_\xi}{\partial t^2} &\approx \frac{U^{n+1}_{\nu,k} - 2U^n_{\nu,k} + U^{n-1}_{\nu,k}}{(\Delta t)^2}, \\
\frac{\partial^2 U_\xi}{\partial \xi_1 \partial \xi_2} &\approx \frac{U^n_{\nu+1,k+1} - U^n_{\nu-1,k+1} - U^n_{\nu+1,k-1} + U^n_{\nu-1,k-1}}{2\Delta\xi_1\Delta\xi_2}, \\
\frac{\partial^2 U_\xi}{\partial \xi_1^2} &\approx \frac{U^n_{\nu+1,k} - 2U^n_{\nu,k} + U^n_{\nu-1,k}}{(\Delta\xi_1)^2}, \\
\frac{\partial^2 U_\xi}{\partial \xi_2^2} &\approx \frac{U^n_{\nu,k+1} - 2U^n_{\nu,k} + U^n_{\nu,k-1}}{(\Delta\xi_2)^2}, \\
\frac{\partial U_\xi}{\partial \xi_1} &\approx \frac{U^n_{\nu+1,k} - U^n_{\nu-1,k}}{2\Delta\xi_1}, \\
\frac{\partial U_\xi}{\partial \xi_2} &\approx \frac{U^n_{\nu,k+1} - U^n_{\nu,k-1}}{2\Delta\xi_2},
\end{aligned} \tag{1.16}$$

where n, ν, and k are the discretization variables for t, ξ_1, and ξ_2, respectively.

The system of equations (1.16) replaced in the acoustic wave equation (1.1) with $F_\xi = 0$ produces the recursive scheme

$$\begin{aligned}
U^{n+1}_{\nu,k} &= -U^{n-1}_{\nu,k} - \frac{\Delta t^2 v_\xi^2}{2\Delta\xi_1^2\Delta\xi_2^2}\Big[-\Delta\xi_1\Delta\xi_2 U^n_{\nu-1,k-1} g_{12} + \Delta\xi_1\Delta\xi_2 U^n_{\nu-1,k+1} g_{12} \\
&+ \Delta\xi_1\Delta\xi_2 U^n_{\nu+1,k-1} g_{12} - \Delta\xi_1\Delta\xi_2 U^n_{\nu+1,k+1} g_{12} \\
&+ U^n_{\nu,k}(-4\Delta\xi_1^2\Delta\xi_2^2 + 4\Delta\xi_2^2 g_{11} + 4\Delta\xi_2^2 g_{22}) \\
&+ (U^n_{\nu+1,k} + U^n_{\nu-1,k})(-2\Delta\xi_2^2 g_{11} - \Delta\xi_1\Delta\xi_2^2\zeta_1) \\
&+ (U^n_{\nu,k+1} + U^n_{\nu,k-1})(-2\Delta\xi_1^2 g_{22} - \Delta\xi_1^2\Delta\xi_2\zeta_2)\Big],
\end{aligned} \tag{1.17}$$

valid up to order two in space and time. We derived a similar expression up

to fourth order in space and second order in time to implement the RTM and FWI algorithm. This results are shown in chapter 3 an 4 respectively.

CHAPTER 2

REVERSE TIME MIGRATION IN RIEMANNIAN MANIFOLDS

The RTM algorithm in Riemannian manifolds for domains with curved boundary has been proposed recently (Shragge, 2014a). Shragge claims that modeling curved domains with rectangular meshes introduce ladder effects that produces artifacts in RTM images. In order to describe the curved domain with a curved mesh Shragge proposes a geometrical transformation known as the Schwarz–Christoffel transformation, a complex variable transformation for 2D domains. Shragge finished the complete RTM algorithm using this scheme but could not extend it to 3D domains because of the nature of the Schwarz–Christoffel transformation. A more general approach to solve the acoustic wave equation in curved domains was introduced by Shargge (2014b) in which a 3d acoustic wave equation was solved in a rectangular domain, that is the transformed to the curved domain via a 3D transformation. In that paper he only shows the propagation but not the RTM. Here we use that transformation to obtain the results for RTM in Riemannian manifolds and compare them with RTM in Cartesian coordinates.

As explained in chapter 2, the wave equation in the Riemannian manifold takes the form:

$$\nabla_{\xi}^{2} U_{\xi} - \frac{1}{v_{\xi}^{2}} \frac{\partial^{2} U_{\xi}}{\partial t^{2}} = F_{\xi}, \tag{2.1}$$

where the Laplacian is modified to include the effect of the transformation of coordinates which induce a metric tensor:

$$\nabla_{\xi}^{2} = \sum_{j=1}^{2} \sum_{l=1}^{2} \frac{1}{\sqrt{|\mathbf{g}|}} \frac{\partial}{\partial \xi_{j}} \left(g^{jl} \sqrt{|\mathbf{g}|} \frac{\partial}{\partial \xi_{l}} \right). \tag{2.2}$$

This Laplacian can be expanded in the form

$$\nabla^2_\xi = \sum_{j=1}^{2}\sum_{l=1}^{2}\left[g^{jl}\frac{\partial^2}{\partial\xi_j\partial\xi_l}\right] + \zeta^1\frac{\partial}{\partial\xi_1} + \zeta^2\frac{\partial}{\partial\xi_2}, \tag{2.3}$$

in order to make easier the numerical calculation since in this way the derivatives have geometrical factors (g^{ij} and ζ^i) that are calculated once and for all at the beginning. The numerical values of these geometrical coefficients are shown in Figures 2.1, 2.2 and 2.3. In general the metric coefficients can be functions of 2 variables for the 2-dimensional RTM so it is common to plot them as 2D maps. (and it can be seen from equation 10 of chapter 1 that the metric coefficient g^{11} is equal to 1 for the particular transformation we are using).

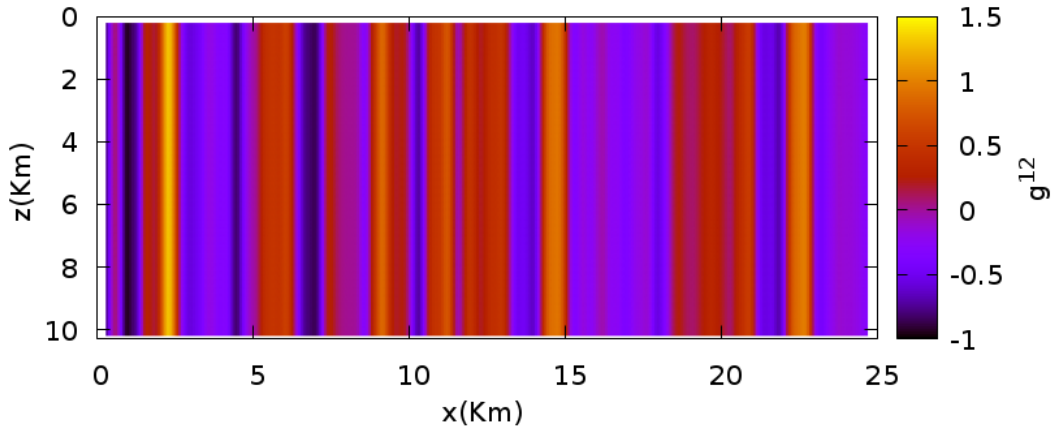

Figure 2.1: Metric coeficient g_{12} corresponding to the mountain profile shown in figure 2.6.

Using the expression (2.3) for the Laplacian we can solve the wave equation (2.1) in the computational domain. The forward propagation, backward propagation and imaging condition can all be done in the regular grid. To obtain the RTM image $I(x_1, x_2)$ we can use the standard zero lag cross correlation between the forward propagated field P_f and the backward propagated field P_b:

$$I(\xi_1, \xi_2) = \sum_s \sum_r \int dt P_f(\xi_1, \xi_2, t) P_b(\xi_1, \xi_2, t) \tag{2.4}$$

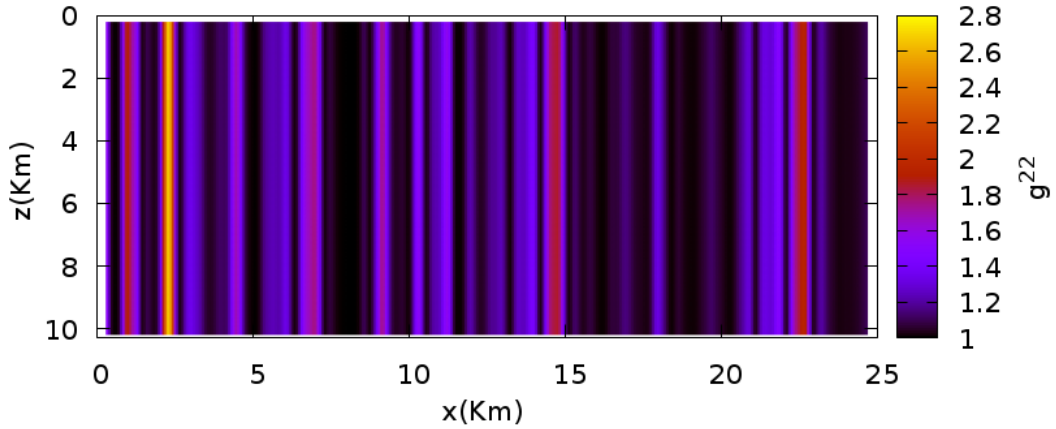

Figure 2.2: Metric coeficient g_{22} corresponding to the mountain profile shown in figure 2.6.

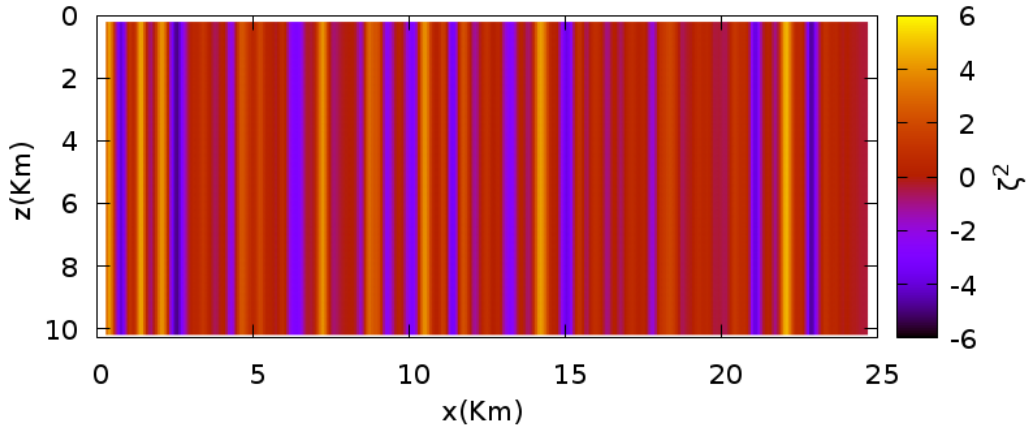

Figure 2.3: Metric coeficient ζ_2 corresponding to the mountain profile shown in figure 2.6.

where the first sum over all sources, the second is over all receptors and the integral is over time. The image $I(x_1, x_2)$ can be obtained form $I(\xi_1, \xi_2)$ just by transforming the arguments from (ξ_1, ξ_2) to (x_1, x_2) using the transformation equations (1.9).

We begin our RTM numerical experiments with a model of 2 layers of constant velocity separated by a straight horizontal interface. The velocity of the

upper layer is 4Km/s and the other is 5Km/s. The step sizes for these grids were $dx = 0.075$Km and $dz = 0.05$Km. The time step was 0.001s. The source used was a Ricker pulse with a central frequency of 6Hz. The number of seismic waves was 24 receivers. All the computational experiments of this chapter were obtained with algorithms implemented in C and parallelized with the standard Message Passing Interface (MPI) for execution in a cluster.

In the side and lower boundaries we used absorbing boundary conditions, and in the upper border we use a rigid boundary condition (the field in the boundary is zero) for simplicity, i.e., we set the wave field over the border equal to zero.

This numerical experiment is done in order to examine the details of the image obtained with RTM in Riemannian coordinates since it is a good starting point. The interface of the 2 layers is placed at 5Km deep. The RTM result for the Riemannian algorithm is shown in Figure 2.4 while the result of the purely Cartesian version is shown in Figure 2.5. The upper curved border should be smoothed in the Riemannian case since the calculation of the metric tensor implies the computation of the derivative along the surface topography. We smoothed it using a simple moving average that assigns to a point in the mountain border a mean height calculated by the expression

$$b_i = (a_{i-1} + a_i + a_{i+1})/3, \tag{2.5}$$

where b_i is the new height assigned to the point i that had a height a_i.

We repeated this smoothing process 10 times to obtain the mountain profile shown in Figure 2.5. If we apply this smoothing process a few times, for example 2 times, the smoothness is not enough and the derivatives of the profile

will have huge values. We also experimented applying cubic splines or Bezier curves to the mountain profile expecting to get more precise result but the results were not much better. The mountain profile of Figure 2.5 on the contrary is the exact profile of the mountain in the sub-sampled Canadian Foothills model.

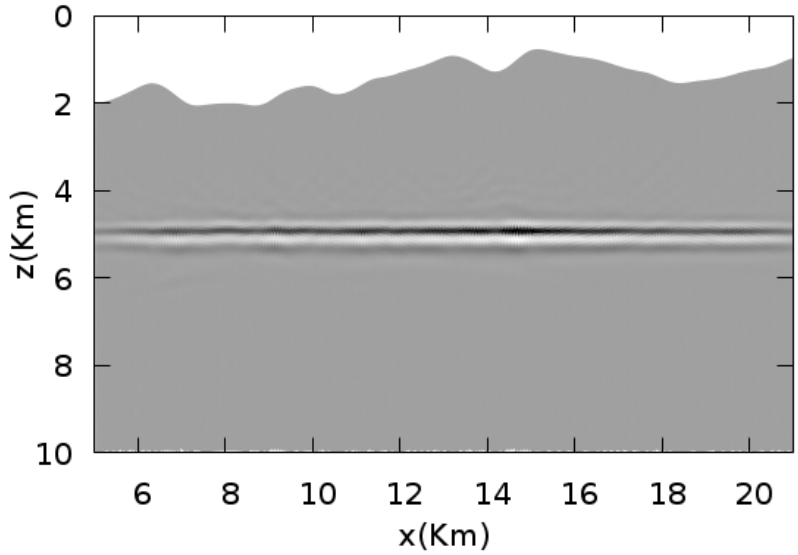

Figure 2.4: RTM image computed with the Riemannian coordinats for a 2 layers model with an upper boundary that corresponds to the Canadian Foothills.

Comparing the figures 2.4 and 2.5 it is evident that the RTM image for the Riemannian coordinates present a reflecting interface less straight than the image corresponding to the Cartesian case. On one hand this is due to the distortion of the seismic waves due to effects of numerical dispersion, an effect that will be analyzed in Chapter 4, and on the other hand due to the fact that in a curved mesh it is harder to represent the straight line corresponding to the plane interface. The Cartesian image shows some shadows (or *artifacts*) in places away from the interface (the interface is the only region were we expect to see something in this case). These artifacts can be produced by the multiple reflections

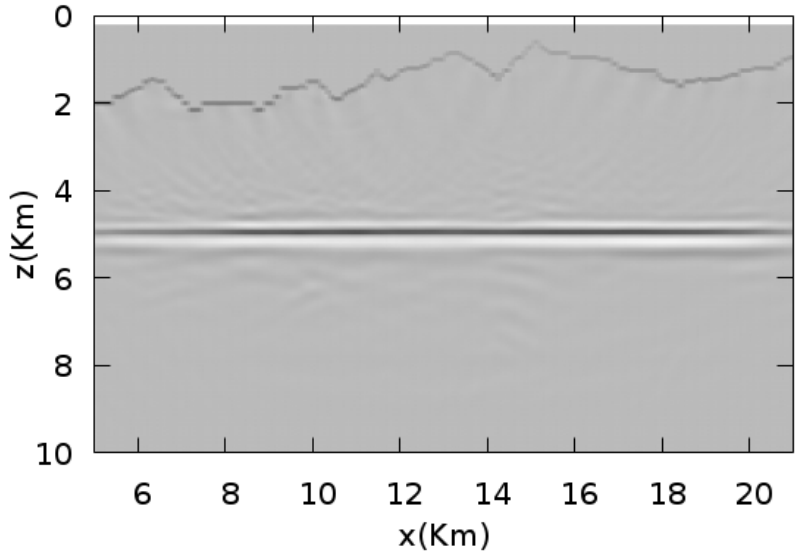

Figure 2.5: RTM image computed with the Cartesian coordiantes for a 2 layers model with an upper boundary that corresponds to the Canadian Foothills.

of the waves over the border of the mountain. Since in the Riemannian scenario the border is smooth, it is natural to expect less artifacts there.

The next numerical experiment involves the sub-sampled Canadian Foothills velocity model shown in Figure 2.6 (Gray and Marfurt, 1995), a synthetic model for a zone in British Columbia that shows several complex structures common in that region of Canada . This model will be transformed into the Riemannian domain, i.e., the computational domain, using the transformation rule given by the equation 1.9. The transformed model in shown in the Figure 2.7.

The RTM image for the Cartesian case is shown in Figure 2.8, and the image

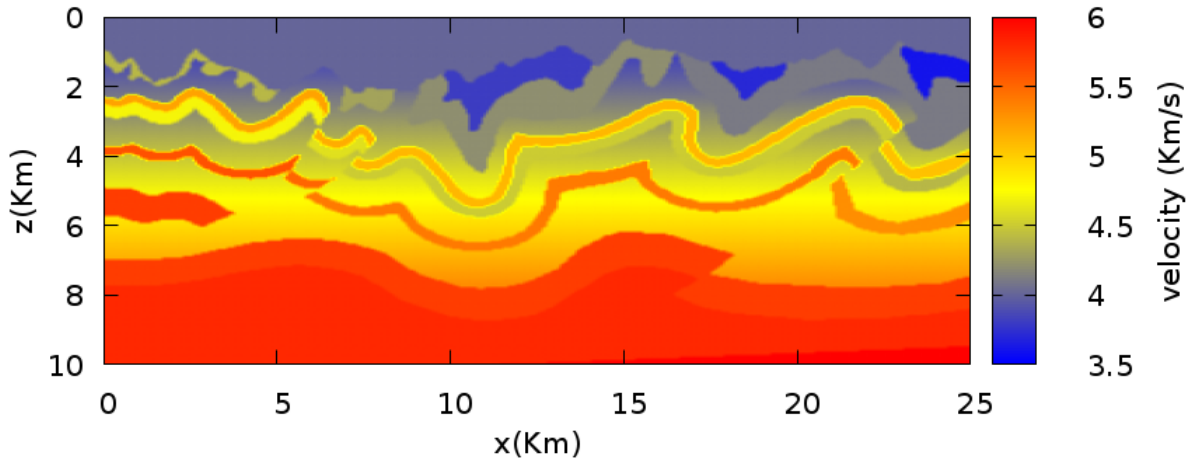

Figure 2.6: The Canadian Foothills. This is a sub-sampled version has $334x200$ sampling points. The original model has $1169x1000$ sampling points

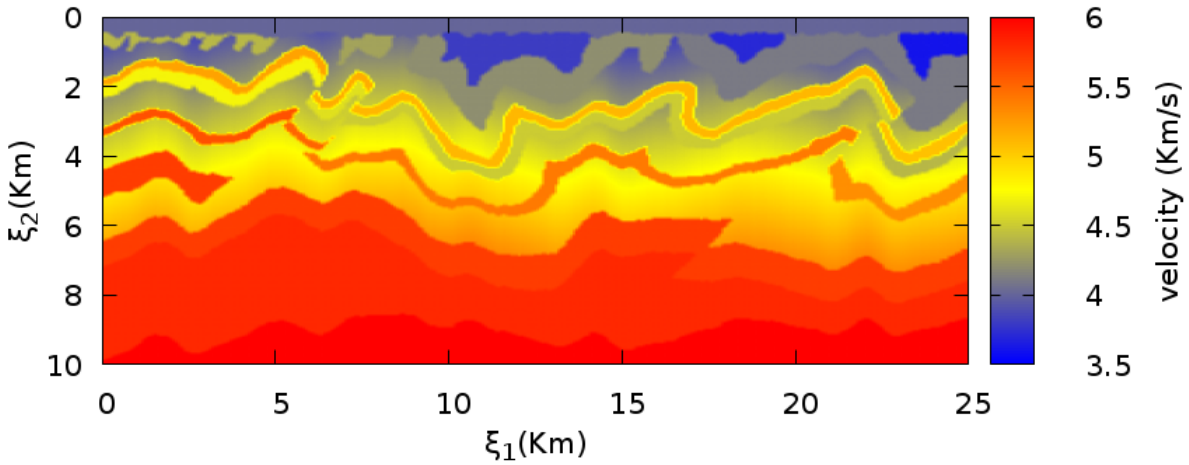

Figure 2.7: Transformation of the Canadian Foothills model into the computational domain. The mountain profile of figure 2.6 is mapped into a horizontal line and all the points below are deformed in a similar way

for the Riemannian case is shown in the Figure 2.9. The values of dx, dz, dt, frequency and the size of the grid are the same that we used for the case of the Figures 2.4, and 2.5

Comparing the Figures 2.8 and 2.9 we see that there is no visible improve-

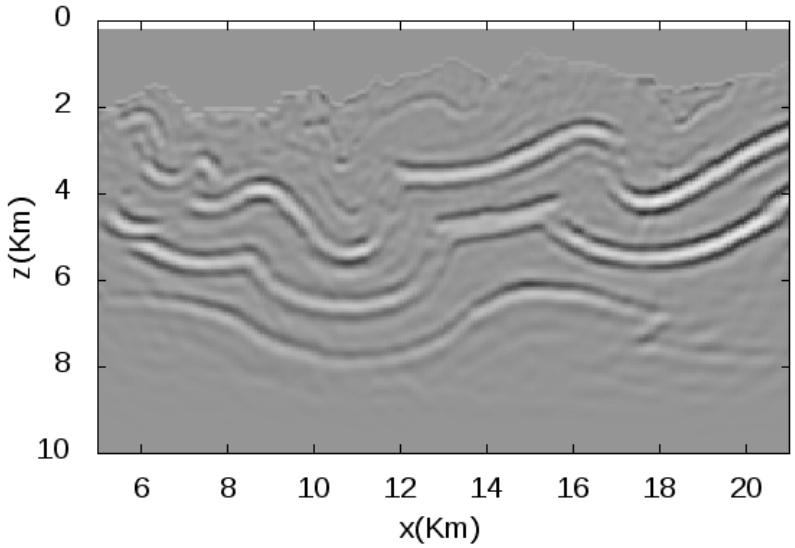

Figure 2.8: RTM image for sub-sampled Canadian Foothills velocity model in the Cartesian scenario.This is a sub-sampled version of size 334x200

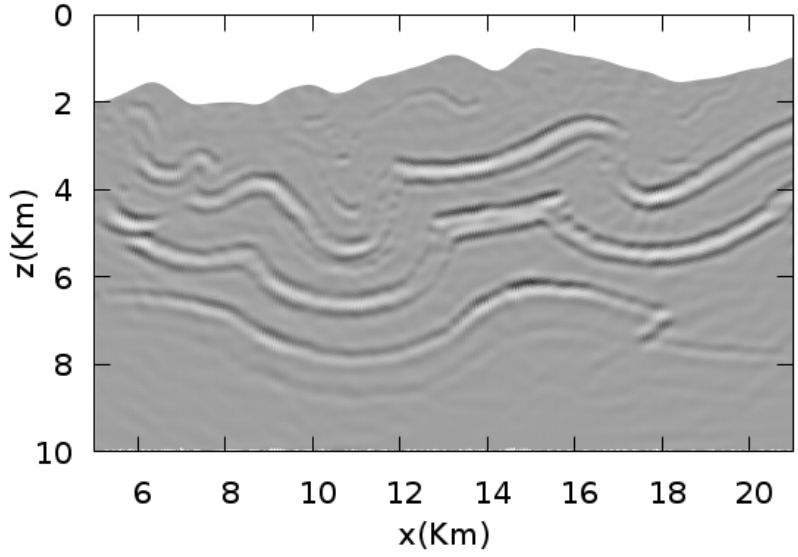

Figure 2.9: RTM image for sub-sampled Canadian Foothills velocity model in the Riemannian scenario.This is a sub-sampled version of size 334x200

ment for the image in the Riemannian scenario as was expected. The near surface details of the Cartesian image seem to be better and the amplitude of the image of the reflector is more continuous too. It is not true furthermore that the curved grid if more suitable to describe the scenarios with rugged topography since as we said before, and we will explain in more detail in the Chapter 4, the mountain border in the Riemannian domain is not the original one but a smoothed version. Although we used the same set of parameters to construct both images, we show in Chapter 4 that this is not in general true. More specifically, there we show that the time step size requires for the stability condition in the curved mesh implies a higher computational cost in the Riemannian case. We applied the Cartesian RTM algorithm to section of the full model (no subsampled) that is shown in Figure 2.10. The result is shown in Figure 2.11. A analog image using the Riemannian scenario was not possible to do because the time sampling required was not practical.

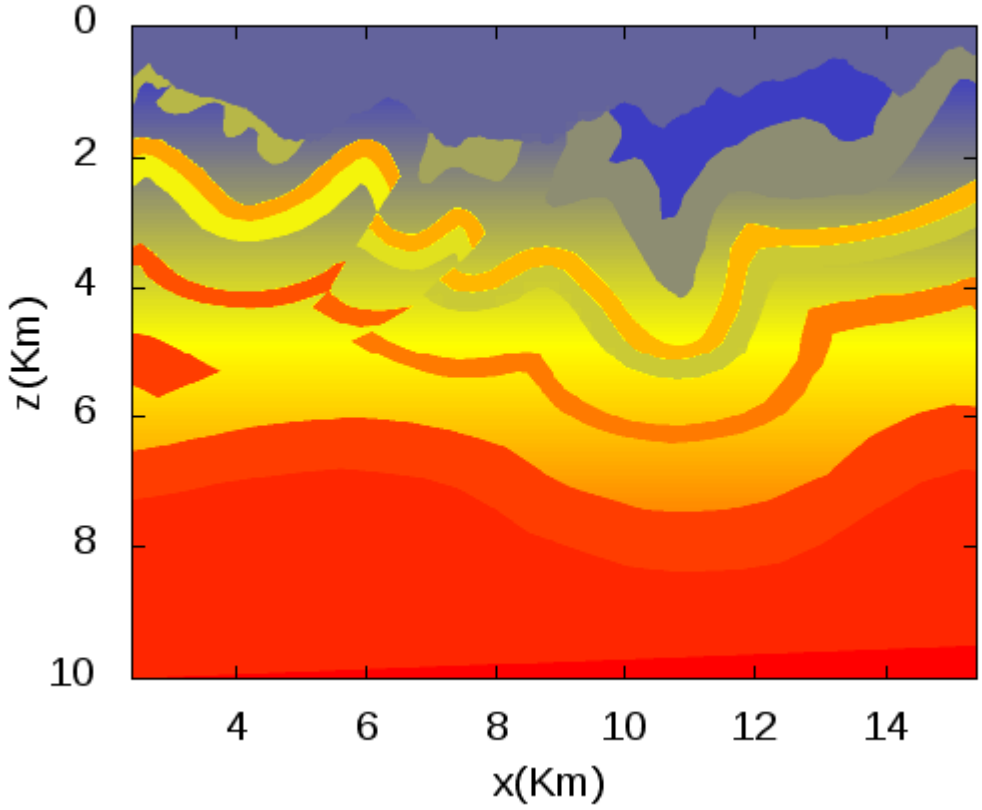

Figure 2.10: A section of the Canadian foothills model

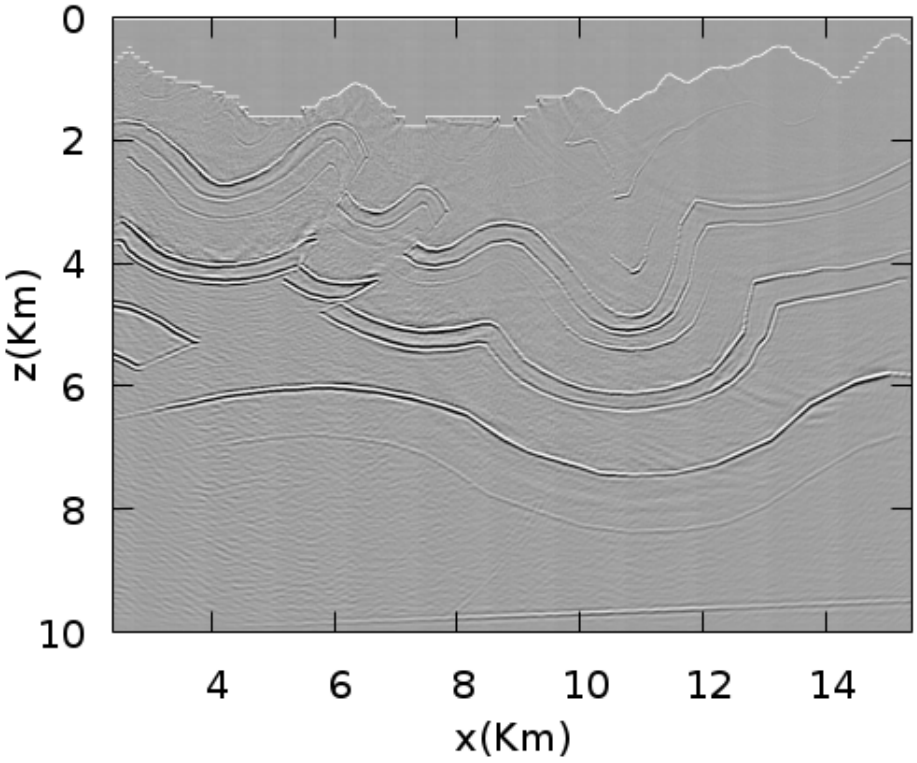

Figure 2.11: RTM image for the model shown in Figure 2.10. This result was calculated with the Cartesian algorithm

CHAPTER 3

FULL WAVEFORM INVERSION IN RIEMANNIAN MANIFOLDS

3.1 Introduction: The standard FWI in Cartesian coordinates

FWI algorithms improve the velocity model of the earth's sub-surface that can be used to create RTM images. This improved velocity model is obtained in an iterative way. In the first step a starting velocity model $\mathbf{m}_0$ is proposed and in each iteration the velocity model is modified adding to it a small variation $\Delta\mathbf{m}$. The improvement of the model in each iteration is measured by means of the quadratic norm of the difference between the real seismogram and the seismogram simulated using the previous velocity model. The expression for this difference is denoted as $E(\mathbf{m})$ and is known as objective function, misfit function, cost function or error function and has the form

$$E(\mathbf{m}) = \frac{1}{2}\sum_{r=1}^{n_g}\sum_{s=1}^{n_s}\int_0^{t_{max}} dt\,|p_{cal}(\mathbf{x}_r, t; \mathbf{x_s}) - p_{obs}(\mathbf{x}_r, t; \mathbf{x_s})|^2\,. \tag{3.1}$$

Here p_{cal} is the wave field calculated at the positions $\mathbf{x}_r$ of the registers (geophones) with the velocity model $\mathbf{m}_0$ and p_{obs} is the observed wave filed, i.e., the field registered by the receivers. To take into account that there are several source positions, the vector variable $\mathbf{x_s}$ is used . All this means that the misfit function is the square of the difference between the real seismogram and the seismogram calculated with the approximated model $\mathbf{m}_0$ .The model variation required to decrease this error can be obtained from the equation (3.1) after some mathematical manipulations that we will review here.

The first step is to take the second-order Taylor expansion of the misfit func-

tion around $\mathbf{m}_0$:

$$E(\mathbf{m}_0 + \Delta\mathbf{m}) = E(\mathbf{m}_0) + \sum_i \frac{\partial E(\mathbf{m}_0)}{\partial m_i}\Delta m_i + \sum_i \sum_j \frac{\partial^2 E(\mathbf{m}_0)}{\partial m_i \partial m_j}\Delta m_i \Delta m_j + O(\|\Delta\mathbf{m}\|^3). \quad (3.2)$$

Here m_i represent the value of the velocity model in the i-th point of the grid. For a $100x100$ grid for example, there will be 10000 model parameters m_i to calculate. In this particular case the optimum set of model parameters should be found by finding the global minimum of the misfit function in a space of 10000 variables. A big question is, how to avoid falling into a local minimum when trying to find the global minimum? This adds complexity to the FWI algorithm which already requires a large amount of computational resources when applied to realistic velocity models.

Taking the derivative with respect to the model parameters m_i results in

$$\frac{\partial E(\mathbf{m})}{\partial m_i} = \frac{\partial E(\mathbf{m}_0)}{\partial m_i} + \sum_j \frac{\partial^2 E(\mathbf{m}_0)}{\partial m_i \partial m_j}\Delta m_j, \quad (3.3)$$

that can be written in a short way as

$$\frac{\partial E(\mathbf{m})}{\partial m_i} = \frac{\partial E(\mathbf{m}_0)}{\partial \mathbf{m}} + \frac{\partial^2 E(\mathbf{m}_0)}{\partial m^2}\Delta\mathbf{m}. \quad (3.4)$$

Then,

$$\Delta\mathbf{m} = -\left(\frac{\partial^2 E(\mathbf{m}_0)}{\partial m^2}\right)^{-1} \frac{\partial E(\mathbf{m}_0)}{\partial \mathbf{m}} = -\mathbf{H}^{-1}\nabla E_{\mathbf{m}} \quad (3.5)$$

where $\mathbf{H}$ is known as the Hessian matrix and $\nabla E_{\mathbf{m}}$ is the gradient of the misfit function that can be written as

$$\nabla E_{\mathbf{m}} = \frac{\partial E(\mathbf{m}_0)}{\partial \mathbf{m}} = \left[\frac{\partial E(\mathbf{m}_0)}{\partial m_1}, \frac{\partial E(\mathbf{m}_0)}{\partial m_2}, ..., \frac{\partial E(\mathbf{m}_0)}{\partial m_N}\right]^T. \quad (3.6)$$

A first approximation used in FWI is to take the Hessian matrix proportional to the identity. In this case the expression for the change in velocity model is

$$\Delta\mathbf{m} = -\alpha\nabla E_{\mathbf{m}} \quad (3.7)$$

where α the constant of proportionality. This means that to vary the velocity model we should move in a direction opposite to the gradient and α fixes the size of the jump in that direction. This technique is known like the gradient or steepest descent method.

Even in the case of a small grid of size $100x100$ the calculation on the gradient in equation (3.6) seem to be rather involved since it is the variation with respect to 10000 parameters. However, the gradient can be calculated by means of integral methods using the equation (Plessix, 2006)

$$\frac{\partial E(\mathbf{m})}{\partial m_i} = \sum_{r=1}^{n_g} \sum_{s=1}^{n_s} \int dt \left[\left(\frac{\partial^2 p(\mathbf{x}, t; \mathbf{x}_s)}{\partial t^2} \frac{2}{m^3(\mathbf{x})} \right) (\Delta p_{res}) \right], \tag{3.8}$$

where Δp_{res} is the residual seismogram, i.e., the difference between the real and calculated seismograms.

So, once the gradient is calculated the new model in each step can be obtained:

$$\mathbf{m}_{k+1} = \mathbf{m}_k + \Delta \mathbf{m}_k \tag{3.9}$$

$$\Delta m_i = -\alpha_k \frac{\partial E_k(\mathbf{m})}{\partial m_i} \tag{3.10}$$

$$\tag{3.11}$$

for $k = 0, 1, 2...N_{iterations}$.

The number $N_{iterations}$ is chosen such that the misfit functions lies below a desired value.

It is convenient to choose an adaptive α because a small constant α can lead

to a very slow convergence and a big value to α can lead to divergence. An optimum value is given by (Liu et al. (2012))

$$\alpha_k = \frac{\sum_s \delta E_k^s E_k^s}{\sum_s \delta E_k^s \delta E_k^s} \tag{3.12}$$

where s is the shot number, k is the iteration number and

$$E_k^s = E^s(\mathbf{m}_k), \tag{3.13}$$

$$\Delta E_k^s = \bar{E}_{k+1}^s - E_k^s, \tag{3.14}$$

$$\bar{E}_{k+1}^s = E^s(\mathbf{m}_k - \nabla E_k). \tag{3.15}$$

3.2 Riemannian FWI

We evaluated the performance of the FWI method in generalized coordinates using the sub-sampled Canadian Foothills synthetic velocity model. The computational grid of the computational experiment is 334×200, with $\Delta x_1 = \Delta x_2 = 0.03$ Km. The mountain profile was smoothed using a moving average. We used 7 point sources of Ricker shape. The FWI had a multi-scale strategy where the Ricker sources and the seismograms have central frequencies 3Hz, 5Hz , 10Hz and 15Hz. In the multi-scale strategy, the estimated velocity model obtained for first frequency is the used as starting-point for the second frequency. For each wave propagation we used a sampling time of 1ms and a total acquisition time of 2.5s. The number of iterations for each frequency was 200. The initial velocity is shown in Figure (3.1). The final estimated model for the first, second and third frequencies are shown in Figures (3.1), (3.2) and (3.3) respectively. As the velocity has originally a flat bottom, the curved mesh must

go beyond. Therefore, the missing area of the curved mesh is filled with a constant velocity 6km/s, which does not harm the results because those points are mainly immersed in the attenuation layer and this does not imply a significant variation for the velocities. The border of the original model was smoothed before any computation. The observed data were generated synthetically using the original model shown in Figure (3.4). These results were obtained with an algorithm parallelized with CUDA-C.

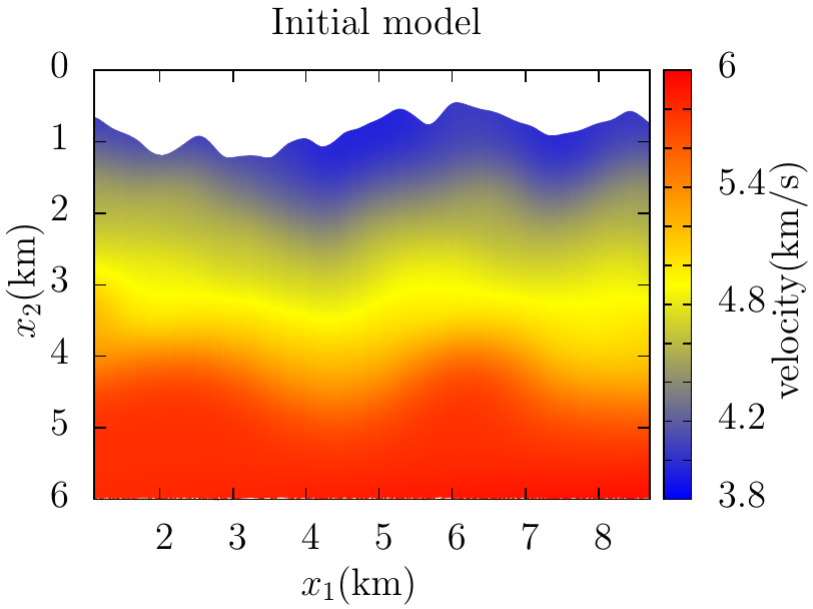

Figure 3.1: The starting velocity model

These numerical experiments show that the multi-scale FWI algorithm in Riemannian coordinates produced a final result quite similar to the original model even with a starting model that was quite far from the original one. The computational cost was moderate since the time sampling is not too far from the one given by the CFL condition Courant condition for this set of parameters which is 3ms, nevertheless this moderate time sampling is not guaranteed for bigger grids or for strong variations on the topography as we show in Chapter 4. It would be interesting to compare the convergence performance of this

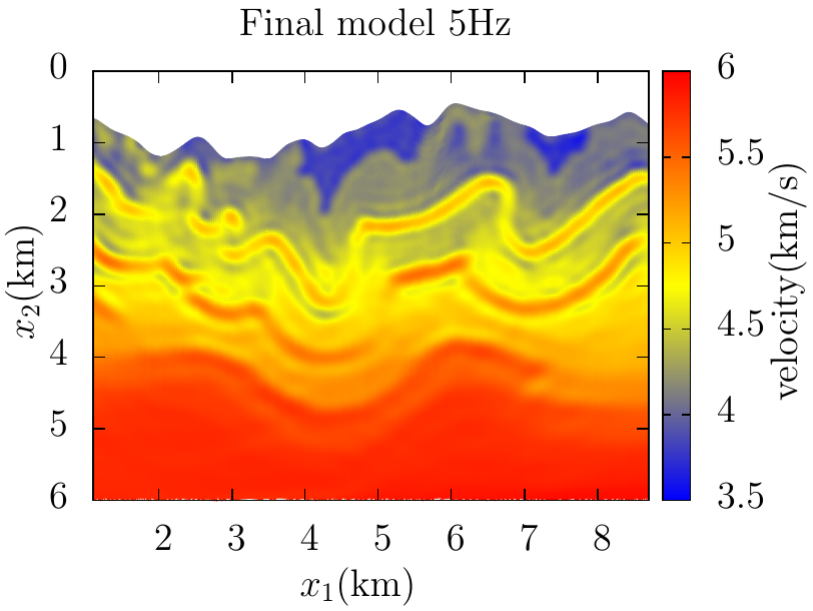

Figure 3.2: The final velocity model with 5hz

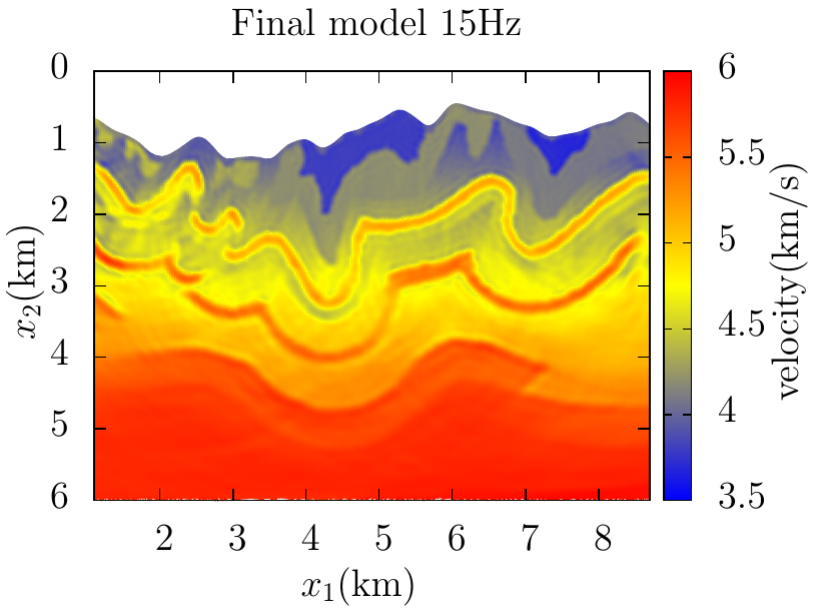

Figure 3.3: The final velocity model with 15hz

algorithm with other ones developed for the same model but in Cartesian coordinates and homogeneous grid.

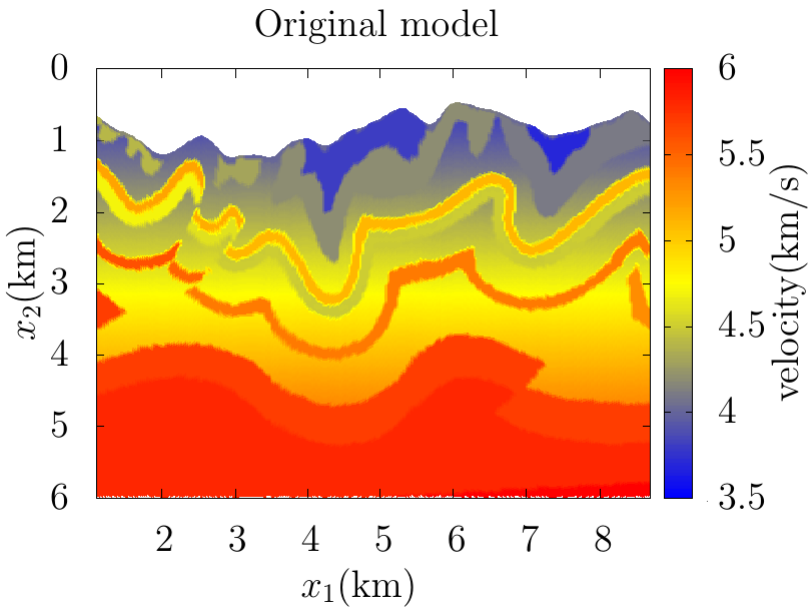

Figure 3.4: The original velocity model

CHAPTER 4

ANALYSIS OF STABILITY AND DISPERSION

4.1 2D-second order Riemannian wave equation FD scheme

The finite-difference method is the most widespread numerical approach in seismic modeling due to its relative accuracy and straightforward implementation, nevertheless, the size of the time step is bounded by a stability criterion which is an important factor affecting the accuracy and the computational effort to obtain the results. This bound depends on the grid spacing and wave speed, particularly for the Riemannian 2D wave equation, it also depends on geometrical factors.

Von-Neumann stability criteria of Riemannian 2D wave equation

The stability condition for the acoustic wave equation is widely known as the Courant-Friderichs-Lewy condition (CFL) and is given in the case of two spatial dimensions by

$$\Delta t \leq \frac{\Delta r}{v(\mathbf{x})}, \tag{4.1}$$

where

$$\Delta r = \left[\Delta x_1^{-2} + \Delta x_2^{-2}\right]^{-\frac{1}{2}} \tag{4.2}$$

is the root-mean-square (RMS) of the spatial sampling and $v(\mathbf{x})$ is the value maximum of the velocity model in physical grid.

In the Riemannian case the only approach to it has been made by Shragge (2014a) who uses the chain rule to go from Equation (4.1) to the following expression:

$$\Delta t \leq \frac{1}{v_{\xi}} \times \underset{\xi}{\operatorname{argmin}} \left\{ \left[\left(\frac{\partial \phi_1}{\partial \boldsymbol{\xi}^T} \Delta \boldsymbol{\xi} \right)^{-2} + \left(\frac{\partial \phi_2}{\partial \boldsymbol{\xi}^T} \Delta \boldsymbol{\xi} \right)^{-2} \right]^{-\frac{1}{2}} \right\}. \tag{4.3}$$

To derive the appropriate stability condition we make use of the Von-Neumann method as follows:

The differential operators in Equation (1.8), expanded in a second order finite difference scheme are:

$$\begin{aligned}
\frac{\partial^2 U_{\xi}}{\partial t^2} &\approx \frac{U^{n+1}_{\nu,k} - 2U^{n}_{\nu,k} + U^{n-1}_{\nu,k}}{(\Delta t)^2}, \\
\frac{\partial^2 U_{\xi}}{\partial \xi_1 \partial \xi_2} &\approx \frac{U^{n}_{\nu+1,k+1} - U^{n}_{\nu-1,k+1} - U^{n}_{\nu+1,k-1} + U^{n}_{\nu-1,k-1}}{2\Delta\xi_1 \Delta\xi_2}, \\
\frac{\partial^2 U_{\xi}}{\partial \xi_1^2} &\approx \frac{U^{n}_{\nu+1,k} - 2U^{n}_{\nu,k} + U^{n}_{\nu-1,k}}{(\Delta\xi_1)^2}, \\
\frac{\partial^2 U_{\xi}}{\partial \xi_2^2} &\approx \frac{U^{n}_{\nu,k+1} - 2U^{n}_{\nu,k} + U^{n}_{\nu,k-1}}{(\Delta\xi_2)^2}, \\
\frac{\partial U_{\xi}}{\partial \xi_1} &\approx \frac{U^{n}_{\nu+1,k} - U^{n}_{\nu-1,k}}{2\Delta\xi_1}, \\
\frac{\partial U_{\xi}}{\partial \xi_2} &\approx \frac{U^{n}_{\nu,k+1} - U^{n}_{\nu,k-1}}{2\Delta\xi_2},
\end{aligned} \tag{4.4}$$

where n, ν, and k are the discretization variables for t, ξ_1, and ξ_2, respectively.

The system of equations (4.4) substituted into the acoustic wave equation (2.1) with $F_{\xi} = 0$ produces the recursive scheme

$$
\begin{aligned}
U^{n+1}_{\nu,k} &= -U^{n-1}_{\nu,k} - \frac{\Delta t^2 v_\xi^2}{2\Delta\xi_1^2\Delta\xi_2^2}\Big[-\Delta\xi_1\Delta\xi_2 U^n_{\nu-1,k-1} g_{12} + \Delta\xi_1\Delta\xi_2 U^n_{\nu-1,k+1} g_{12} \\
&+ \Delta\xi_1\Delta\xi_2 U^n_{\nu+1,k-1} g_{12} - \Delta\xi_1\Delta\xi_2 U^n_{\nu+1,k+1} g_{12} \\
&+ U^n_{\nu,k}(-4\Delta\xi_1^2\Delta\xi_2^2 + 4\Delta\xi_2^2 g_{11} + 4\Delta\xi_2^2 g_{22}) \\
&+ (U^n_{\nu+1,k} + U^n_{\nu-1,k})(-2\Delta\xi_2^2 g_{11} - \Delta\xi_1\Delta\xi_2^2\zeta_1) \\
&+ (U^n_{\nu,k+1} + U^n_{\nu,k-1})(-2\Delta\xi_1^2 g_{22} - \Delta\xi_1^2\Delta\xi_2\zeta_2)\Big], \qquad (4.5)
\end{aligned}
$$

valid up to order two in space and time. Now consider a trial solution in the form

$$
U^n_{\nu,k} = u^n_{\nu,k} + \epsilon^n_{\nu,k}\,, \qquad (4.6)
$$

where U_ξ is the exact solution (if it exists), u is the approximation to the solution and ϵ is the error introduced up to the desired order when approximating the solution. Assuming that equation (4.5) has solutions of the form

$$
u^n_{\nu,k} = u^n e^{i(\kappa_1 \nu\Delta\xi_1 + \kappa_2 k\Delta\xi_2)}\,, \qquad (4.7)
$$

where $i = \sqrt{-1}$ is the imaginary number and κ_1, and κ_2 are wave numbers, we can expect that the error behaves in the same way:

$$
\epsilon^n_{\nu,k} = \epsilon^n e^{i(\kappa_1 \nu\Delta\xi_1 + \kappa_2 k\Delta\xi_2)}\,. \qquad (4.8)
$$

Inserting Equation (4.6) in the FD scheme Equation (4.5) and taking into account that u satisfies the wave equation within the specified order of accuracy , the resulting equation only involves ϵ:

$$
\begin{aligned}
\epsilon^{n+1}_{\nu,k} &= 2\epsilon^n_{\nu,k} - \epsilon^{n-1}_{\nu,k} \\
&+\epsilon^n_{\nu,k}(c\Delta t)^2\left(\frac{\zeta^1}{\Delta\xi_1} i\sin(\kappa_1\Delta\xi_1) + \frac{\zeta^2}{\Delta\xi_2} i\sin(\kappa_2\Delta\xi_2) + \frac{g^{11}}{(\Delta\xi_1)^2}[2\cos(\kappa_1\Delta\xi_1) - 2]\right. \\
&\left. + \frac{g^{22}}{(\Delta\xi_2)^2}[2\cos(\kappa_2\Delta\xi_2) - 2] + \frac{g^{12}}{2\Delta\xi_1\Delta\xi_2} 2i\sin(\kappa_1\Delta\xi_1) 2i\sin(\kappa_2\Delta\xi_2)\right), \qquad (4.9)
\end{aligned}
$$

that can be written as

$$\epsilon^{n+1} = B\epsilon^n - \epsilon^{n-1}\,. \tag{4.10}$$

Denote

$$R = \frac{\epsilon^{n+1}}{\epsilon^n} = \frac{\epsilon^n}{\epsilon^{n-1}}\,, \tag{4.11}$$

then the previous expression is written as $R^2 - BR + 1 = 0$, from which

$$R = \frac{B \pm \sqrt{B^2 - 4}}{2}\,. \tag{4.12}$$

We want ϵ^n, to remain bounded, so $|R| \leq 1$ which implies that the stability condition for the 2D Riemannian wave equation is

$$\left|B \pm \sqrt{B^2 - 4}\right| \leq 2. \tag{4.13}$$

If B were real, this expression could be replaced by two inequalities that would allow us to solve for Δt but In this case, however, we have that B is complex, so that our strategy is to evaluate this inequality numerically, for a range of values of Δt and take for each value of ξ_1 the maximum value of Δt that satisfies the inequality.

We applied the same procedure to calculate the stability for the generalized acoustic wave equation using finite differences formulas of 4th order for the spatial derivatives. Again we obtained a relation between ϵ^{n+1}, ϵ^n and ϵ^{n-1} because they come from the second derivative in time that is kept at second order in the finite differences approximation. That produces again a polynomial of order 2 for R and then an stability condition similar to (4.13) but the B is a larger expression:

$$
\begin{aligned}
B = 2 \;+\; & v^2(\Delta t)^2 \left\{ \left(\frac{2\cos(\kappa_1\Delta\xi_1)\sin^2\left(\frac{1}{2}\kappa_1\Delta\xi_1\right)}{3\Delta\xi_1^2} - \frac{14\sin^2\left(\frac{1}{2}\kappa_1\Delta\xi_1\right)}{3\Delta\xi_1^2} \right) g_{11} \right. \\
& + \left(\frac{4\sin(2\kappa_1\Delta\xi_1)\sin(\kappa_2\Delta\xi_1)}{9\Delta\xi_1\Delta\xi_2} - \frac{32\sin(\kappa_1\Delta\xi_1)\sin(\kappa_2\Delta\xi_2)}{9\Delta\xi_1\Delta\xi_2} \right. \\
& \left. + \frac{4\sin(\kappa_1\Delta\xi_1)\sin(2\kappa_2\Delta\xi_2)}{9\Delta\xi_1\Delta\xi_2} - \frac{\sin(2\kappa_1\Delta\xi_1)\sin(2\kappa_2\Delta\xi_2)}{18\Delta\xi_1\Delta\xi_2} \right) g_{12} \\
& + \left(\frac{2\cos(\kappa_2\Delta\xi_2)\sin^2\left(\frac{1}{2}\kappa_2\Delta\xi_1\right)}{3\Delta\xi_2^2} - \frac{14\sin^2\left(\frac{1}{2}\kappa_1\Delta\xi_1\right)}{3\Delta\xi_2^2} \right) g_{22} \\
& + i\left(\frac{4\sin(\kappa_1\Delta\xi_1)}{3\Delta\xi_2} - \frac{\sin(2\kappa_1\Delta\xi_1)}{6\Delta\xi_1} \right) \zeta_1 \\
& \left. + i\left(\frac{4\sin(\kappa_2\Delta\xi_2)}{3\Delta\xi_2} - \frac{\sin(2\kappa_2\Delta\xi_2)}{6\Delta\xi_2} \right) \zeta_2 \right\}
\end{aligned} \tag{4.14}
$$

Numerical dispersion analysis

The numerical dispersion analysis is performed observing the relation between the phase velocity and the frequency or what is the equivalent, between phase velocity and the number of points per wavelength (ppw). When there is no dispersion the phase velocity is frequency independent. To find this relation the plane wave solution (4.7) is substituted in the equation (4.5) which, up to order 2, gives the following equation:

$$
e_{\nu,k}^n = e^{i(\kappa_1 \nu\Delta\xi_1 + \kappa_2 k\Delta\xi_2 - \omega n\Delta t)} . \tag{4.15}
$$

To derive the dispersion relation, the harmonic plane wave in Equation (4.15) is used in equations (4.4), and obtain

$$
\begin{aligned}
2\cos(\omega\Delta t) = 2 \;+\; & v^2(\Delta t)^2 \left[\frac{-2g_{11}}{\Delta\xi_1^2} + \frac{2\cos(d\xi_1 p\cos(\theta))g_{11}}{d\xi_1^2} \right. \\
& \left. - \frac{\sin(d\xi_1 p\cos(\theta))\sin(d\xi_2 p\sin(\theta))g_{12}}{d\xi_1 d\xi_2} - \frac{2g_{22}}{d\xi_2} + \frac{2\cos(d\xi_2 p\sin(\theta))g_{22}}{d\xi_2^2} \right.
\end{aligned}
$$

$$
\begin{aligned}
&+ \quad i\frac{\sin(d\xi_1 p\cos(\theta))\zeta_1}{d\xi_1} + i\frac{\sin(d\xi_2 p\sin(\theta))\zeta_2}{d\xi_2}\Bigg] \\
&= \quad f(\xi_1, \theta, \Delta\xi_1, \Delta\xi_2, p),
\end{aligned} \tag{4.16}
$$

where p is the modulus of the wavenumber vector and θ is its argument. Equation (4.16) allows us to find the relation between the grid points per wavelength $G_1 = \lambda/\Delta\xi_1$, $G_2 = \lambda/\Delta\xi_2$ and the normalized phase velocity $C_p/v = (\omega/k)/v$ since

$$
\frac{C_p}{v} = \frac{\omega}{k}\frac{1}{v} = \frac{\omega}{2\pi}\frac{\lambda}{\Delta\xi}\frac{\Delta\xi}{v} = \frac{\omega}{2\pi}G\Delta\xi, \tag{4.17}
$$

$$
p\Delta\xi = \frac{2\pi}{G}, \tag{4.18}
$$

and

$$
\omega\Delta t = \frac{C_p}{v}\frac{2\pi}{G}\frac{v\Delta t}{\Delta\xi} = \frac{C_p}{v}\frac{2\pi c}{G} \tag{4.19}
$$

where $c = v\Delta t/\Delta\xi$ is the Courant-Friedrich-Levy number.

Replacing the expression (4.19) in the equation (4.16) we get

$$
\frac{C_p}{v} = \frac{G}{4\pi c}\arccos(f(\xi_1, \theta, \Delta\xi, p)) \tag{4.20}
$$

where we took $\Delta\xi_1 = \Delta\xi_2 = \Delta\xi$ for simplicity and f is defined in equation (4.16).

4.2 Numerical Results

In this section we investigate, the 2D acoustic wave propagation for two topographic coordinates, in the following aspects: (i) stability criteria, and (ii) numerical dispersion. These computational meshes provide informative tests of the generalized 2D acoustic wave-equation theory and of the implementation of the 2D FDTD numerical scheme described above.

Numerical stability

As a first example we solved the generalized acoustic wave equation (2.1) for a domain with constant velocity and an upper boundary with the form $\psi(x_1) = he^{-a^2x_1^2}$ with $h = 3$ and $a = 0.5$ that is shown in Figure 4.2. A snapshot for the propagation in that domain is shown in Figure 4.1. The stability condition was evaluated numerically using values for Δt from 0.6 s to 0 s and taking the biggest value of Δt that satisfies (4.13) at each point ξ_1. Note that taking into account the transformation (1) $\xi_1 = x_1$ so we can evaluate the stability condition in terms of x_1 directly. The result is shown in Figure 4.3.

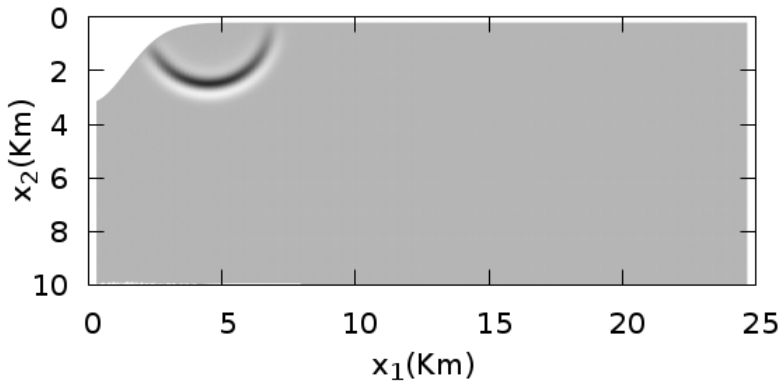

Figure 4.1: Snapshot for the propagation of a Ricker pulse in a medium with constant velocity and a upper boundary with the form $\psi(x_1) = he^{-a^2x_1^2}$. The value of Δt used for the propagation was $4 \times 10^{-3}s$, which is in agreement with the numeric limit shown in Figure 4.3 but not with the heuristic limit

In Figure 4.3 the numeric limit is found by solving numerically the expression (4.13) and the heuristic limit is the one given by the equation (4.3).

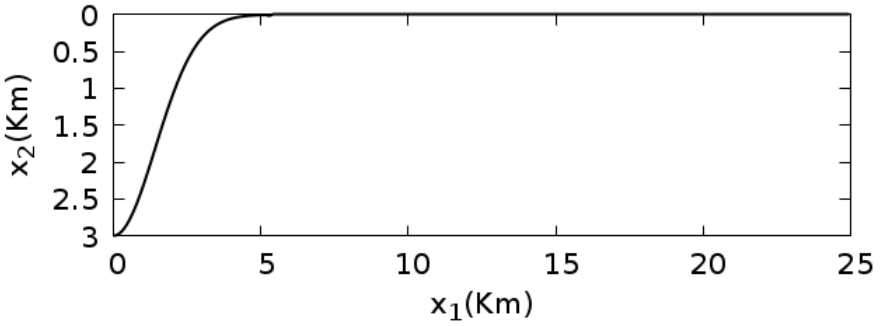

Figure 4.2: Mountain profile with the form $\psi(x_1) = he^{-a^2x_1^2}$

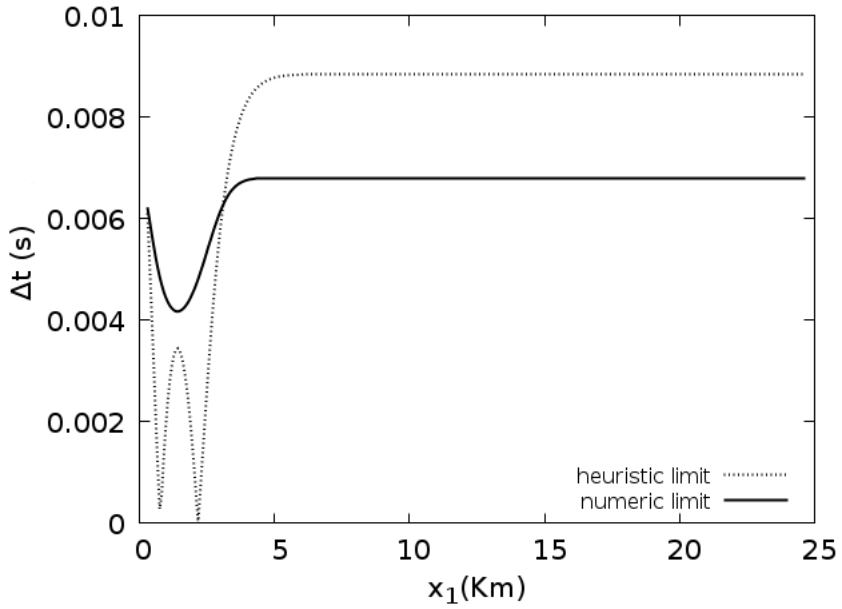

Figure 4.3: Stability condition for the generalized wave equation with an upper border given by an Gaussian form.The solid line corresponds to the numerical solution of the expression 4.13. The minimum Δt for the numeric limit is $4.1 \times 10^{-3} s$ and for the heuristic limit is 1.8×10^{-6}

As a second example we solved the equation (2.1) for a domain with a constant velocity (4 Km/s) and with an upper border corresponding to the Canadian Foothills velocity model. The original model is of size 1668x1000 but for our analysis we used a sub-sampled version, taking one sample for each 5 points of the model in both directions. The sub-sampled version of our velocity model

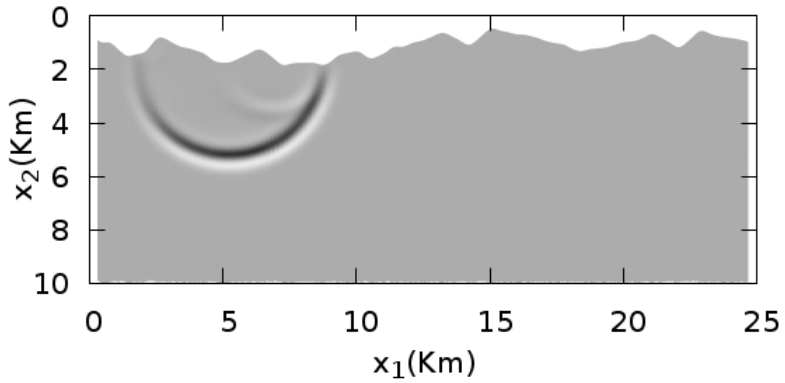

Figure 4.4: Snapshot of the propagation of a Ricker pulse in a constant velocity model with a upper profile corresponding to a sub-sampled version of the Canadian Foothills with size 334x200.The value of Δt used for the propagation was $10^{-3}s$, which is in agreement with the numeric limit shown in Figure 4.7 but not with the heuristic limit. The CFL limit for a Cartesian version of this model would be $5.9 \times 10^{-3}s$ which implies that the computational cost is 143% bigger using the generalized wave equation. The mountain profile was smoothed with a moving average. A secondary wavefront is due to the reflection of the wave in the rugged surface

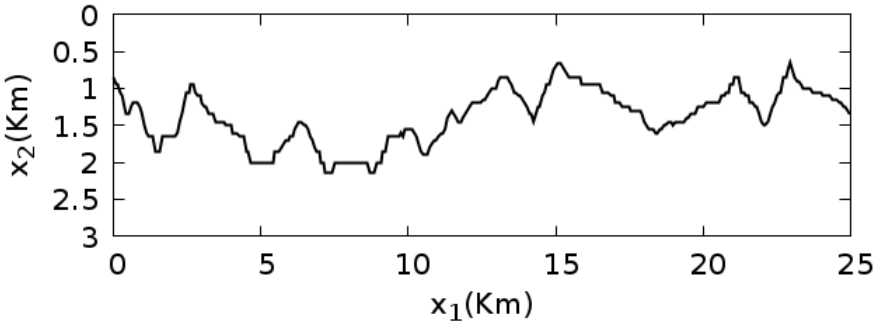

Figure 4.5: Profile corresponding to a sub-sampled version of the Canadian Foothills with size 334x200

is of size 334x200. A snapshot of the propagation of a Ricker pulse in this model is shown in Figure 4.4.

As the calculation of the coefficients ζ_i requires the use of second derivatives, the mountain border should be smooth in order to avoid divergences, so we smoothed the original border of the sub-sampled model that is shown if Figure 4.5 using a simple moving average: the height of each point of the mountain

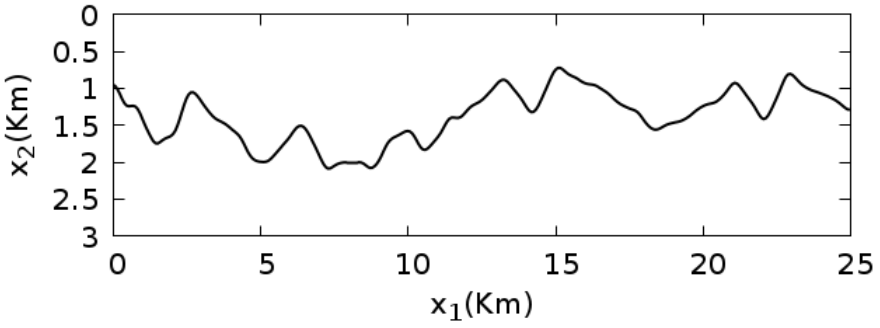

Figure 4.6: Mountain profile for the Canadian Foothills smoothed with a moving average

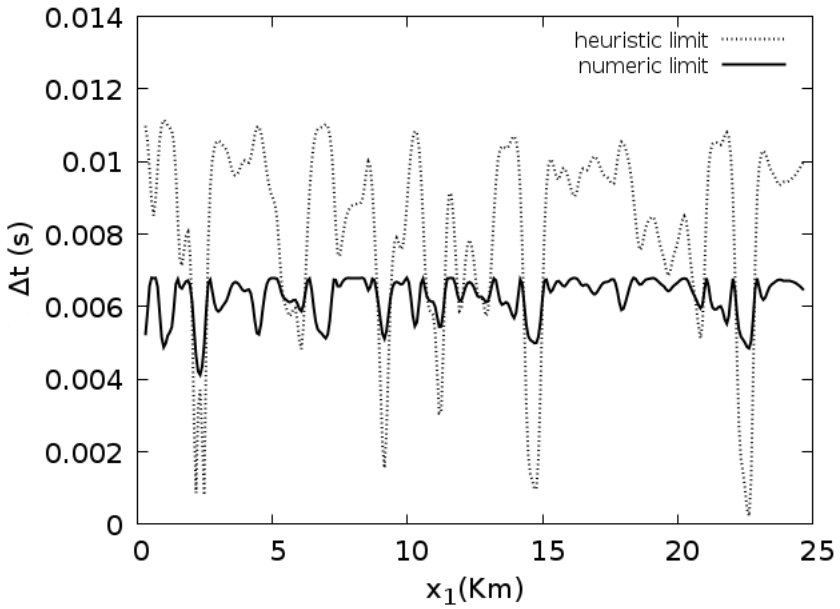

Figure 4.7: Stability condition for the generalized wave equation Canadian Foothill velocity model. The solid line corresponds to the numerical solution of the expression 2.1. The minimum Δt for the numeric limit is $4 \times 10^{-3} s$ and for the heuristic limit is $2 \times 10^{-4} s$

was recalculated as the simple mean of the two nearest neighbors. Figure 4.6 shows the result of the application of this moving average smoothing 5 times. The profile of Figure 4.6 correspond to the one shown in the Figure 4.4. As shown in Figure 4.7 in the the numeric limit for Δt is bigger than the heuristic limit.

Let us define here the *degree of smoothness* of the profile as the number of times it was smoothed with the simple moving average. We evaluated the stability condition (4.13) for different degrees of smoothness for the profile of Figure 4.5 and found that the minimum Δt depends on this degree. The profiles for the several degrees of smoothness we used are shown in Figure 4.8 and the respective limits for Δt are shown in Figure 4.9.

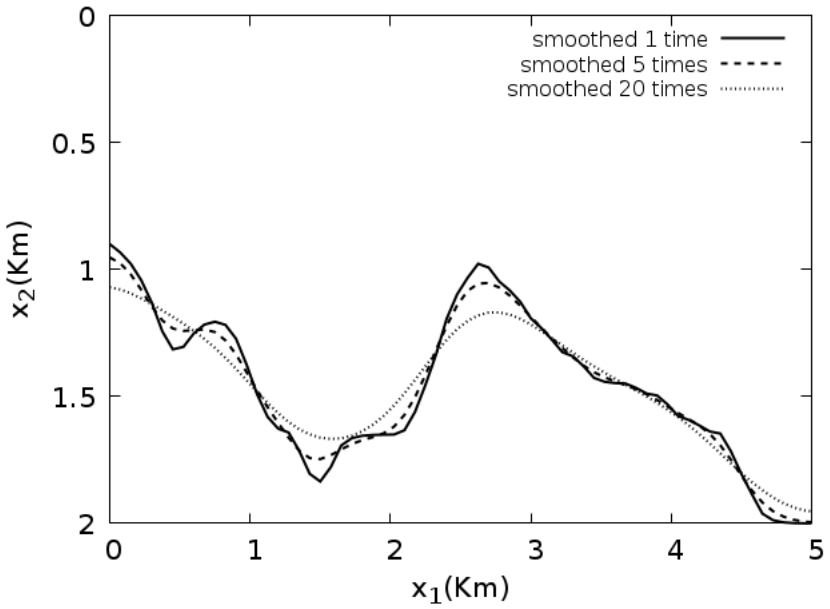

Figure 4.8: Profile for section of the sub-sampled Canadian Foothills model with different amount of smoothness

Additionally we studied the dependence of the condition (4.13) on the frequency and found that the maximum Δt allowed depends strongly on the particular value of the frequency used. For the propagation we used a Ricker pulse of central frequency $6Hz$ but it is obviously composed of a wide range of frequencies. Viewing the power spectrum of this pulse we identified range from $1Hz$ to $80Hz$ approximately so we evaluated (4.13) for different values in this range. The results are shown in Figure 4.10.

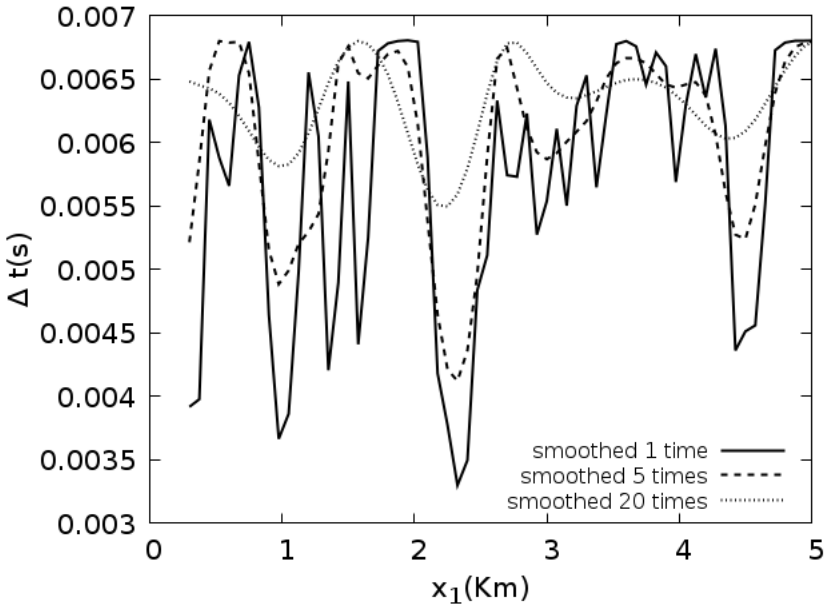

Figure 4.9: Maximum Δt allowed for different degrees of smoothness for a section the sub-sampled Canadian Foothills model. The three stability graphs correspond to the profile of figure 4.5 smoothed 1, 5 and 20 times and the respective limits for Δt are 0.0032 s, 0.0041 s and 0.0054 s

The result for the stability for a section of the Canadian Foothills model at second and fourth order is shown in Figure 4.11.

Dispersion analysis

Finally, we performed a dispersion analysis using the equation (4.20) which allows to observe the variation of the normalized velocity C_p/v as the number of points per wavelength varies. The Figure 13 shows the result when we take the angle $\theta = 0$ for the wavenumber and the Figure 14 shows the result when the angle is $\pi/2$. As comparison we calculated the dispersion for the acoustic

wave equation without metric, i.e., the simple acoustic wave equation and the result, shown in Figure 15 shows a behavior that is expected: that for a number of points per wavelength large enough the normalized velocity tends to 1. In Figure 15 after a value of the grid point per wavelength around 14 the normalized velocity remains stabilized. Contrary to the expected result, Figure 13 shows that no matter the number of point per grid taken, C_p/v is not stabilized which means that different frequencies have different values of the phase velocity C_p producing wavefronts that are deformed as the time runs. This effect is more dramatic for an angle of the wavenumber vector $\theta = \pi/2$ as shown in 14.

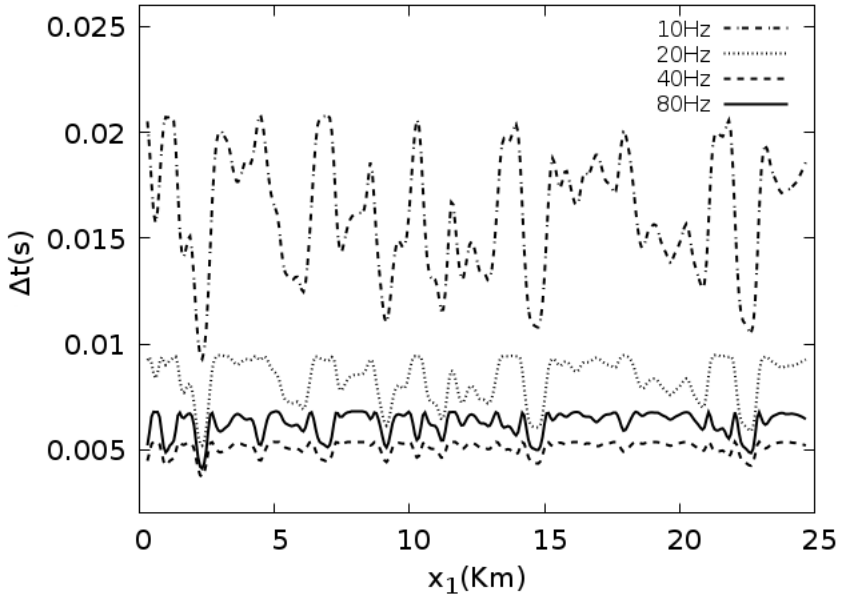

Figure 4.10: Maximum Δt allowed for different frequencies. For frequencies bigger than $80Hz$ the curves lie between those of top and the bottom shown.

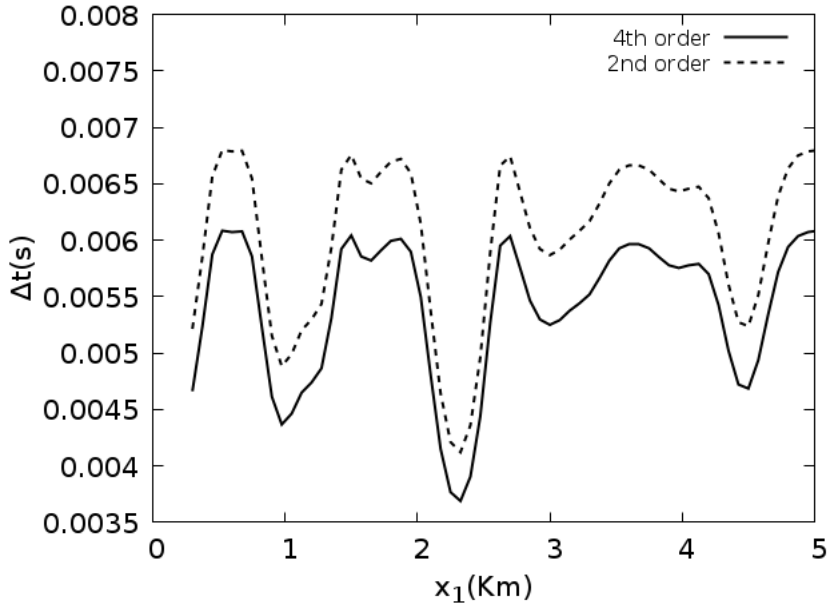

Figure 4.11: Comparison of the stability conditions of order 2 and 4 in the spatial derivatives for the generalized acoustic wave equation. The maximum Δt allowed for the 2nd order scheme is 0.0041 s and for the 4th order is 0.0037 s

4.12

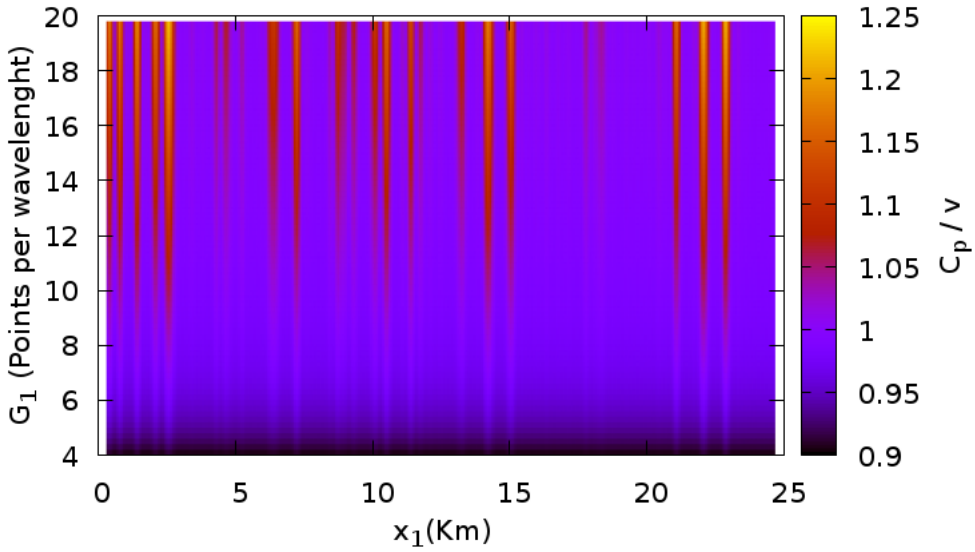

Figure 4.12: Dispersion analysis for the sub-sampled Canadian Foothills model of size 334x200. The graph shows that the normalized velocity C_p/v does not get the expected value of 1 for large numbers grid points per wavelength. This plot is for $\theta = 0$

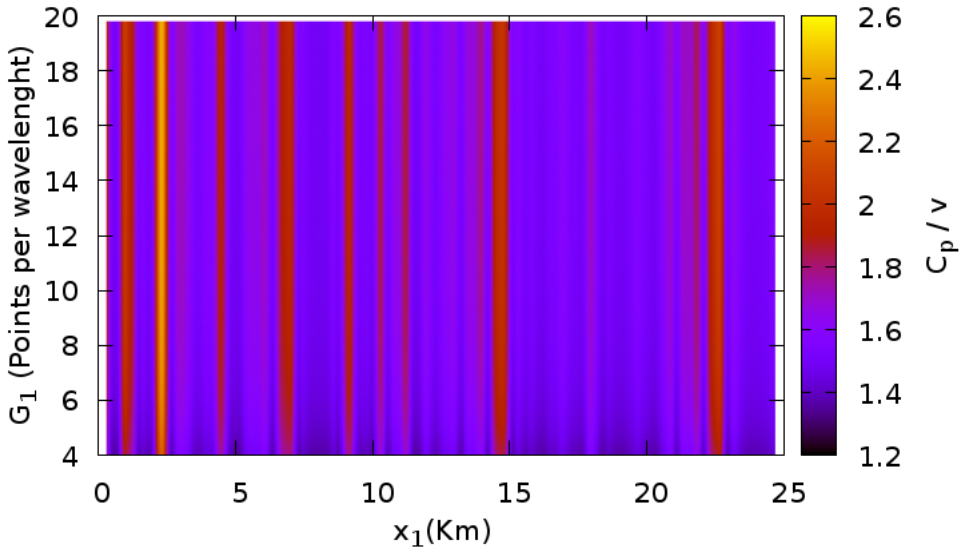

Figure 4.13: Dispersion analysis for the sub-sampled Canadian Foothills model of size 334x200. The graph shows that the normalized velocity C_p/v does not get the expected value of 1 for large numbers grid points per wavelength. This plot is for $\theta = \pi/2$

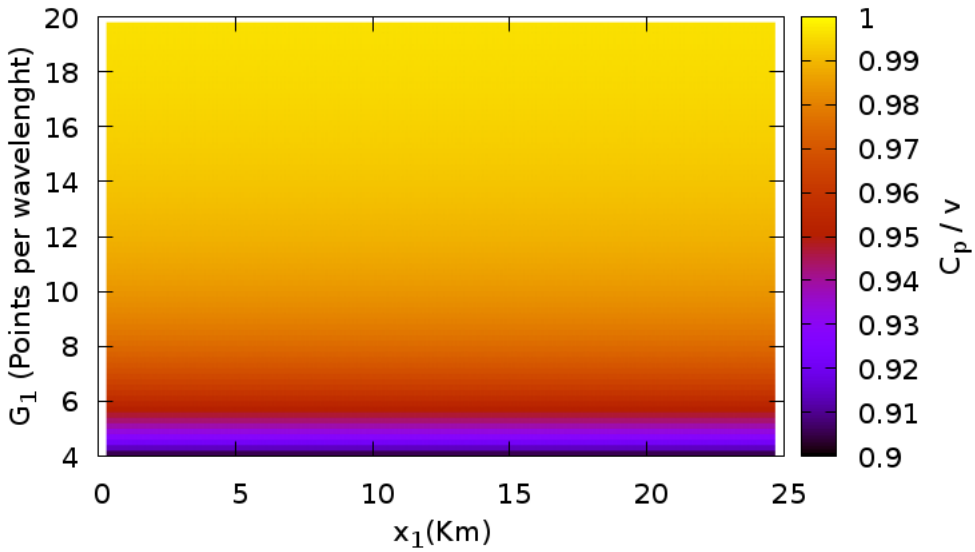

Figure 4.14: Dispersion analysis for a constant velocity model with Cartesian metric and flat surface of size 334x200. The graph shows that the normalized velocity C_p/v get the expected value of 1 for large numbers grid points per wavelength.

CONCLUSIONS

The images obtained by the RTM algorithm in Riemannian coordinates for the sub-sampled velocity model are not better that those obtained in Cartesian coordinates. When we used the Canadian Foothills model without sub-sampling, we could not find a time step for which the Riemannian RTM propagation is stable so we only obtained the RTM in this case for the Cartesian algorithm.
Although the FWI results obtained seem to be promising although this lack of a guarantied stability put the Riemannian method in an obscure scenario.

The numerical experiments show that the time step implied by the stability condition depends strongly on the degree of smoothness of the mountain profile, so that to obtain time steps suitable for calculations we must represent the topography with curves that does not pass exactly for each point of the true profile.

There is a clear difference between the time step given by the heuristic stability condition and the time step given by the limit obtained rigorously.

The limits obtained for the time sampling show that the computational cost of a propagation using the generalized wave equation is in general larger than the same simulation with the usual acoustic wave equation (around 143%) greater than the one for a particular case shown.

Different transformations from the physical domain to the computational domain implies different metric tensors and in turn different limit for the time step required for the stability condition.

This kind of transformations imply very strong numerical dispersion that suggests that the Riemannian approach to the solution of the wave equation does not seem to be convenient for RTM or FWI.

The stability and numerical dispersion analysis for other kind of domain transformation can be achieved using the same general expression given here, just by replacing the corresponding metric tensor.

REFERENCES

Appelo, D. and Petersson, A. (2009). A stable finite difference method for the elastic wave equation on complex geometries with free surfaces. *Commun. Compt.Phys.*, 5(1):84–107.

Claerbout, J. and Doherty, S. (1983). Downward continuation of moveout corrected seismograms. *Geophysics*, 28(60).

D. Loewenthal, L. Lu, R. R. and Sherwood, J. (1976). The wave equation applied to migration. *Geophysical Prospecting*, 24(2).

E. Baysal, D. D. K. and Sherwood, J. W. C. (1983). Reverse time migration. *Geophysics*, 48(11).

Energy education (2015). Oil and gas traps. [Online; accessed June 28, 2017].

Gray, S. H. and Marfurt, K. J. (1995). Migration from topography: Improving the near-surface image. *Can. J. Expl. Geophys*, 31(1):18–24.

Guggenheimer, H. W. (1977). *Differential geometry*. Dover Books on Mathematics.

Liu, F., Guasch, L., Morton, S., Warner, M., Umpleby, A., Meng, Z., Fairhead, S., and Checles, S. (2012). 3d time-domain full waveform inversion of a valhal obc dataset. *SEG Annual International Meeting, Expanded Abstracts*, pages 1–5.

Marsden, J. and Hughes, T. (1983). Mathematical foundations of elasticity. *Dover Publications, INC. New York.*

Plessix, R. (2006). A review of the adjoint-state method for computing the gradient of a functional with geophysical applications. *Geophysics Journal International*, 167(2).

Robin, J. and Salamon, D. (2013). Introduction to differential geometry. *ETH Zurich. Lecture Notes.*

Sahara Wealth Advisors (2015). Seismic imaging. [Online; accessed June 29,

2017].

Sava, P. and Fomel, S. (2005). Riemannian wavefield extrapolation. *Geophysics*, 70(3).

Shragge, J. (2008). Riemannian wavefield extrapolation:nonorthogonal coordinate systems. *Geophysics*, 73(2).

Shragge, J. (2014a). Reverse time migration from topography. *Geophysics*, 79(4).

Shragge, J. (2014b). Solving the 3d acoustic wave equation on generalized structured meshes: A finite-difference time-domain approach. *Geophysics*, 79(1).

Stolt, R. (1978). Migration by fourier transform. *Geophysics*, 79(1).

Tarantola, A. (1984). Inversion of seismic reflection data in the acoustic approximation. *Geophysics*, 49(8).

Virieux, J. and Operto, S. (2009). An overview of full waveform inversion in exploration geophysics. *Geophysics Journal International*, 74(6).

Y. Han, J. Huang, Z. L. and Jia, L. (2015). Acoustic full waveform inversion method research in areas with rugged surface. *SEG Annual International Meeting, Expanded Abstracts*, pages 1356–1360.

Zhao, H., Gao, J., and Chen, Z. (2014). Stability and numerical dispersion analysis of finite-difference method for the diffusive-viscous wave equation. *International Journal of Numerical Analysis and Modeling*, 5(1):66–78.